



20 **Abstract**

21 Optimum performance of irrigated crops in regions with shallow saline groundwater
22 requires a careful balance between application of irrigation water and upward movement
23 of salinity from the groundwater. Few field validated surrogate models are available to
24 aid in the management of irrigation water under shallow groundwater conditions. The
25 objective of this research is to develop a model that can aid in the management using a
26 minimum of input data that is field validated. In this paper a 2-year field experiment was
27 carried out in the Hetao irrigation district in Inner Mongolia, China and a physically based
28 integrated surrogate model for arid irrigated areas with shallow groundwater was
29 developed and validated with the collected field data. The integrated model that links
30 crop growth with available water and salinity in the vadose zone is called Evaluation of
31 the Performance of Irrigated Crops and Soils (EPICS). EPICS recognizes that field capacity
32 is reached when the matric potential is equal to the height above the groundwater table
33 and thus not by a limiting hydraulic conductivity. In the field experiment, soil moisture
34 contents and soil salt conductivity at 5 depths in the top 100 cm, groundwater depth,
35 crop height, and leaf area index were measured in 2017 and 2018. The field results were
36 used for calibration and validation of EPICS. Simulated and observed data fitted
37 generally well during both calibration and validation. The EPICS model that can predict
38 crop growth, soil water, groundwater depth and soil salinity can aid in optimizing water
39 management in irrigation districts with shallow aquifers.

40 **Key words:** Surrogate hydrological model, irrigated crops, shallow aquifer



41 **1. Introduction**

42 Irrigation water is a scarce resource, especially in arid and semi-arid areas of the world.
43 Irrigation improves quality and quantity of food production; however, excess irrigation
44 and salinization remain one of the key challenges. Almost 20% of the irrigated land in
45 the world is affected by salinization and this percentage is still on the rise (Li et al., 2014).
46 Salinity affects agricultural production (Williams, 1999). Soil salinization and water
47 shortages, especially associated with surface irrigated agriculture in arid to semi-arid
48 areas, is a threat to the well-being of local communities in these areas (Dehaan and
49 Taylor, 2002; Rengasamy, 2006).

50 In arid and semi-arid surface irrigation districts without a drainage infrastructure, the
51 groundwater table is close to the surface because more water has been applied than
52 crop evapotranspiration. Capillary rise of the shallow groundwater can be used to
53 supplement irrigation and thereby, in closed basins, can possibly save water for irrigating
54 additional areas downstream (Gao et al., 2015; Yeh and Famiglietti, 2009; Luo and
55 Sophocleous, 2010.). However, at the same time, capillary upward moving water carries
56 salt from the groundwater increasing the salt in the upper layers of the soil leading to
57 soil degradation and possibly decreasing yields and change of crop patterns to more salt
58 tolerant crops (Guo et al., 2018; Huang et al., 2018). Over 50% of the total irrigated
59 cropland, 5250 km² in the Hetao irrigation district in the Yellow River basin, is affected
60 by salinity (Feng et al., 2005). Therefore, understanding the interaction of improved crop
61 yield, soil salinization and decreased surface irrigation is important to the sustainability
62 of the surface irrigation water systems in arid and semi-arid areas. This will require



63 experimentation under realistic farmers' field conditions, as well as modeling to extend
64 the findings beyond the plot scale.

65 Field scale models for water, solute transport and crop growth are widely available.
66 Crop growth models use either empirical functions or model the underlying physiological
67 processes (Liu, 2009). Models widely used for simulating crop growth are EPIC (Williams
68 et al., 1989), DSSAT (Uehara, 1989), WOFOST (Diepen et al., 1989) and AquaCrop
69 (Hsiao et al., 2009; Raes et al., 2009; Steduto et al., 2009). Models focused on water
70 and solute movement in the vadose zone using some form of Richards' equation are
71 HYDRUS (Šimůnek et al., 1998) and SWAP (Dam et al., 1997). Models that integrate crop
72 growth and water-solute movement processes are SWAP-WOFOST (Hu et al., 2019),
73 SWAP-EPIC (Xu et al., 2015; Xu et al., 2016), HYDRUS-EPIC ((Wang et al., 2015), and
74 HYDRUS-DSSAT (Shelia et al., 2018). These integrated models require input data that are
75 usually not available when applied over extended areas (Liu et al., 2009; Xu et al., 2016;
76 Hu et al., 2019). The EPIC crop growth model is often preferred in integrated crop
77 growth hydrology models because it requires relatively few input data and is accurate
78 (Wang et al., 2014; Xu et al., 2013; Chen et al., 2019).

79 There is a tendency with the advancement of computer technology to include more
80 physical processes in these models (Asher et al., 2015; Doherty and Simmons, 2013;
81 Leube et al., 2012). Detailed spatially input of soil hydrological properties and crop
82 growth are required to take advantage of the model complexity (Flint et al., 2002; Rosa
83 et al., 2012). This greater model complexity, both in space and time, requires longer
84 model run times, especially for the time-dependent models (Leube et al., 2012). These



85 models are useful for research purposes but for actual field applications, the required
86 input data are not available and expensive to obtain. In such cases, simpler surrogate
87 models are a good alternative (Blanning, 1975; Willcox and Peraire, 2002; Regis and
88 Shoemaker, 2005). Surrogate models run faster and are as accurate as the complex
89 models for a specific problem (shallow groundwater here) but not as versatile as the
90 more complex models that can be applied over a wide range of conditions (Asher et al.,
91 2015).

92 Simple surrogate models are abundant in China for areas where the groundwater is
93 deeper than approximately 10 m (Kendy et al., 2003; Chen et al., 2010; Ma et al., 2013;
94 Li et al., 2017), but are limited and relatively scarce for areas where the groundwater is
95 near the surface in the arid to semi-arid areas (Xue et al., 2018; Gao et al., 2017; Liu et
96 al., 2019). When the groundwater is deep, the change in matric potential in the subsoil is
97 small and the hydraulic potential is equal to the gravity potential. However, for areas with
98 shallow aquifers (i.e., less than approximately 3 m), the matric potential cannot be
99 ignored. The flow of water is upward when the absolute value of matric potential is
100 greater than the groundwater depth or downward when it is less than the groundwater
101 depth (Gardner, 1958; Gardner et al., 1970a; b; Steenhuis et al., 1988). The field
102 capacity in these soils is reached when the hydraulic gradient is constant (i.e., the
103 constant value of sum of matric potential and gravity potential). In this case, the soil
104 water is in equilibrium and no flow occurs.

105 Because of the shortcomings in the above complex models, the objective of this
106 research was to develop a field validated surrogate model that could be used to optimize



107 both water use efficiency and crop yield in irrigated areas with shallow groundwater and
108 salinized soil with a minimum of input parameters. To validate the surrogate model, we
109 performed a 2-year field experiment in the Hetao irrigation district that investigated the
110 change in soil salinity, moisture content, groundwater depth and maize and sunflower
111 growth during the growing season.

112

113 **2. Model description**

114 2.1 Introduction of the model

115 In a recent study, we presented a surrogate model for the vadose zone with shallow
116 groundwater using the novel concept that the moisture content at field capacity is a
117 unique function of the groundwater depth after irrigation or precipitation that wets up
118 the entire soil profile. The model, called the Shallow Vadose Groundwater model, applies
119 directly to surface irrigated districts where the groundwater is within 3.3 m from the soil
120 surface (Liu et al. 2019). The model was a proof of concept with calibrated values for
121 evapotranspiration and soil salinity and was not simulated.

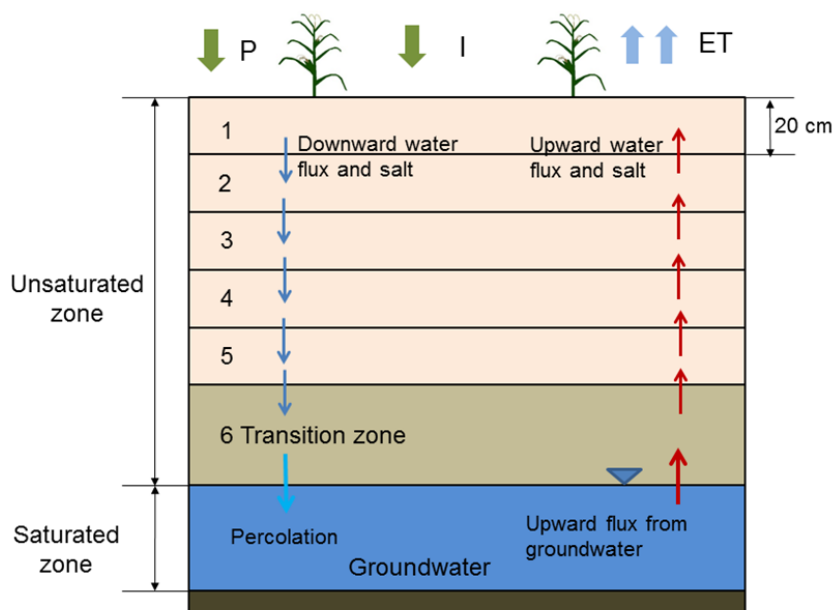
122 To make the Shallow Vadose Groundwater model more physically realistic, we added
123 a crop growth model and included the effect of salinity and moisture content on
124 evaporation and transpiration directly in this study. The new model that combines parts
125 of the Environmental Policy Integrated Climate (EPIC) with Shallow Vadose Groundwater
126 model is called the *Evaluation of the Performance of Irrigated Crops and Soils* (EPICS).

127 2.2 Structure of the EPICS model

128 In the EPICS model, the soil profile is divided into five layers of 20 cm (from the soil



129 surface down) and a sixth layer that stretches from the 100 cm depth to the water table
 130 below (Fig. 1).



131

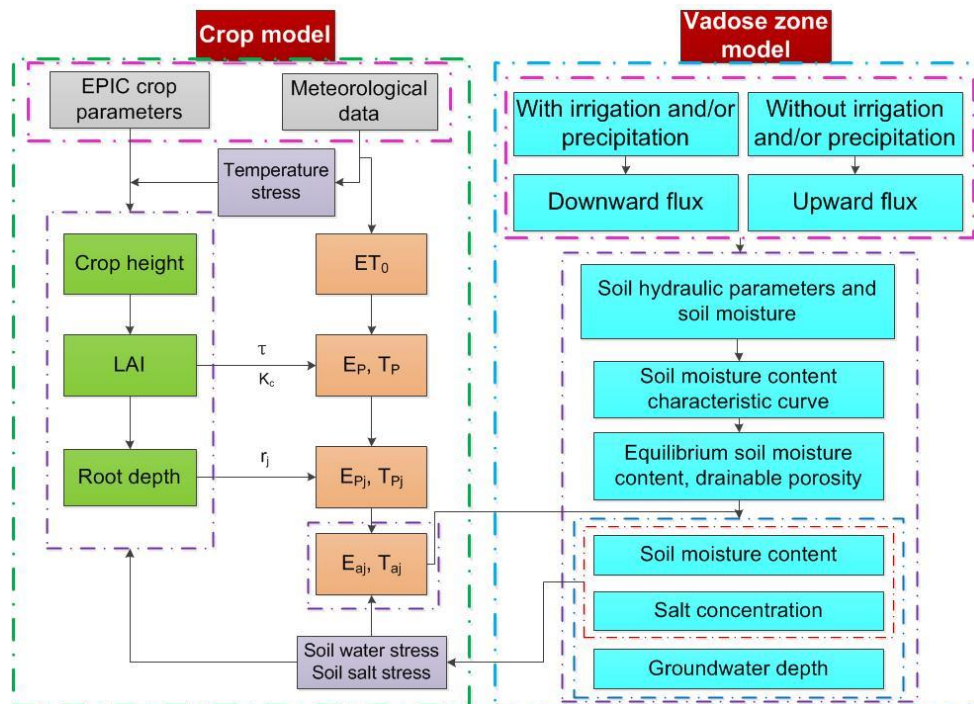
132 Fig 1. Schematic diagram of model components and water movement

133

134 The moisture content and salt content are calculated for each day (Fig.1). All flow
 135 takes place within the day and the water and salt content are in “equilibrium” (i.e., fluxes
 136 are zero) at the end of the day for which the calculations are made. Daily fluxes
 137 considered in the vadose model are the following: at the surface, the fluxes are irrigation,
 138 both irrigation water, $I(t)$, and salt, $S_{\alpha}(t)$, and precipitation, $P(t)$, and for each layer, j , on
 139 days with irrigation and rainfall, the downward flux of water, $R_w(j,t)$, and salt, $S(j,t)$,
 140 between the layers. On days without water input at the soil surface, an upward
 141 groundwater flux $U(j,h,t)$, and salt, $S(j,t)$ are considered. The flux to the surface depends
 142 on the groundwater depth. Finally, transpiration, $T(j,t)$, removes water from the layers
 with roots of the crops and evaporation, $E(j,t)$, from all layers.



143 The EPICS model consists of two modules: the VADOSE module and the CROP
 144 module. The two modules are linked through the evapotranspiration flux in the soil (Fig.
 145 2).



146
 147 Fig 2. Schematic diagram of the linked novel Shallow Aquifer-Vadose zone surrogate
 148 module and EPIC module. Note: ET_0 is the reference evapotranspiration, E_p and T_p are the
 149 potential evaporation and potential transpiration, E_a and T_a are the actual evaporation
 150 and actual transpiration, K_c is the crop coefficient, τ is the development stage of the leaf
 151 canopy, and r_j is the root function of soil layer j .

152
 153 The CROP module employs functions of the EPIC model (Williams et al., 1989) and
 154 root growth distribution (Novak, 1987; Kendy et al., 2003; Chen et al. 2019). The CROP
 155 module calculates daily values of crop height, root depth and leaf area index (LAI) based
 156 on climatic data (Fig. 2).

157 The VADOSE module calculates the moisture and salt content in the root zone and



158 the upward movement of the groundwater (Fig.2). Field capacity varies with depth and is
159 a function of the (shallow) groundwater depth and the soil characteristic curve (Liu et al.,
160 2019). Moisture contents become less than field capacity when the upward flux is less
161 than the actual evapotranspiration.

162 Finally, the link between the VADOSE and the CROP modules is achieved by
163 calculating the actual evapotranspiration with parameters of both modules consisting of
164 the moisture content and the salt content simulated in the VADOSE module and root
165 distribution and potential evapotranspiration in the CROP module (Fig. 2).

166 2.3 Theoretical background of the EPICS model

167 In the next section, the equations of the CROP in the VADOSE modules are presented.
168 The calculations are carried out sequentially on a daily time step. Finer resolution is not
169 needed for managing water and salt content for irrigation. In the first step, the actual
170 evaporation and transpiration are calculated for each layer in the model. Next, the
171 moisture content and salt content are adjusted for the various fluxes. Since the equations
172 for the downward movement on days of rainfall and/or irrigation are different than for
173 upward movement from the groundwater on the remaining days, we present upward and
174 downward movement in separate sections. The code was written in Matlab 2014a and
175 Microsoft Excel was used for data input and output.

176 2.3.1 CROP module

177 The crop module uses functions of EPIC (Erosion Productivity Impact Calculator, Williams
178 et al., 1989) to calculate leaf area index, LAI, crop height and the root depth (green



179 boxes in Fig. 2), and the potential transpiration, T , and evaporation, E (orange boxes in
 180 Fig. 2). Input data for the CROP module included: mean daily temperature (T_{mean}),
 181 maximum daily temperature (T_{mx}), minimum daily temperature (T_{mn}), maximum crop height
 182 (H_{mx}), maximum LAI (LAI_{mx}), maximum root depth (RD_{mx}), dimensionless canopy extinction
 183 coefficient (K_b), and total potential heat units required for crop maturation (PHU).

184 The potential rates of evaporation, $E_p(j, t)$, and transpiration, $T_p(j, t)$, of different
 185 layers are derived from the total rates and a root function that determines the
 186 distribution of roots in the vadose zone

$$187 \quad T_p(j, t) = r_T(j, t)T_p(t) \quad (1a)$$

$$188 \quad E_p(j, t) = r_E(j, t)E_p(t) \quad (1b)$$

189 where the letters in the parenthesis are the independent variables on which the
 190 parameter before the parenthesis depends, $T_p(t)$ is the total potential transpiration and
 191 $E_p(t)$ is the total potential transpiration at time, t . Both are calculated with the CROP
 192 module (S1 in the supplementary material). Root functions (Sau et al., 2004; Delonge et
 193 al., 2012) were used to calculate transpiration and evaporation of different soil layer.
 194 $r_T(j, t)$ is the root function for the transpiration and $r_E(j, t)$ is the root function for the
 195 evaporation. Both have the same general equation but with a different value for the
 196 constant δ .

$$197 \quad r_T(j, t) = \left[\frac{1}{1 - \exp(-\delta)} \right] \left\{ \exp \left[-\delta \left(\frac{Z_{1j}}{Z_{2j}} \right) \right] \left[1 - \exp \left(-\delta \frac{Z_{2j} - Z_{1j}}{Z_r} \right) \right] \right\} \quad (2a)$$

$$198 \quad r_E(j, t) = \left[\frac{1}{1 - \exp(-\delta)} \right] \left\{ \exp \left[-\delta \left(\frac{Z_{1j}}{Z_{2j}} \right) \right] \left[1 - \exp \left(-\delta \frac{Z_{2j} - Z_{1j}}{Z_r} \right) \right] \right\} \quad (2b)$$

199 Where z_j is the depth of the upper boundaries of the soil layer j . For $r_T(j, t)$ if the root



200 depth is smaller than the lower boundaries of the soil layer j , Z_{2j} is equal to the root
 201 depth and if the root depth is greater than the lower boundaries of the soil layer j , Z_{2j} is
 202 the depth of the lower boundaries of the soil layer j . For $r_E(j, t)$, Z_{2j} is depth of the
 203 lower boundaries of the soil layer j . Z_r is the root zone depth and δ is the water use
 204 distribution parameter. Note that the sum of $r_T(j, t)$ of all soil layers is equal to 1. In the
 205 study of Novark (1987), the value of δ for corn is 3.64 and we used this value. To obtain
 206 $r_E(j, t)$, δ was set to 10 (Chen et al., 2019; Kendy et al., 2003). Sunflower root function
 207 simulation employed the same δ values as for maize.

208 The actual evaporation rates, $E_a(j, t)$, and transpiration, $T_a(j, t)$, for each soil layer, j ,
 209 at time, t , are calculated as a proportion of the potential values as:

$$210 \quad E_a(j, t) = k_E(j, t)E_p(j, t) \quad (3a)$$

$$211 \quad T_a(j, t) = k_T(j, t)S(j, t)T_p(j, t) \quad (3b)$$

212 where $k_E(j)$ and $k_T(j)$ are water stress coefficients and $S(j)$ is a salt stress coefficient.

213 According to Raes et al. (2009), the water stress coefficients are

$$214 \quad k_E(j, t) = \exp\left(-2.5 \frac{\theta_{0.33}(j) - \theta(j, t)}{\theta_{0.33}(j) - \theta_{15}(j)}\right) \quad \theta \leq \theta_{0.33} \quad (4a)$$

$$215 \quad k_E(j, t) = 1 \quad \theta > \theta_{0.33} \quad (4b)$$

216 where $\theta_{0.33}(j)$ is the moisture content at 0.33 bar or -33 kPa for layer j , or when the

217 conductivity becomes limiting and $\theta_{15}(j)$ is the moisture content at wilting point 15 bar

218 (1.5 Mpa), $\theta(j, t)$ is the soil moisture content for layer j at time t .

219 Then water stress coefficient in Eq. 3b is:

$$220 \quad k_T(j, t) = 1 - \frac{\exp\left[\left(1 - \frac{\theta(j, t) - \theta_{15}(j)}{(1-p)[\theta_{0.33}(j) - \theta_{15}(j)]}\right) f_{shape}\right] - 1}{\exp(f_{shape}) - 1} \quad \theta \leq \theta_{0.33} \quad (5a)$$

$$221 \quad k_T(j, t) = 1 \quad \theta > \theta_{0.33} \quad (5b)$$



222 where f_{shape} is the shape factor of $k_T(j, t)$ curve, p is the fraction of readily available
223 soil water relative to the total available soil water. Finally, the salt stress coefficient
224 $S(j, t)$ for each layer in Eq 3b can be calculated as (Allen et al., 1998; Xue et al., 2018):

$$225 \quad S(j, t) = 1 - \frac{B}{100 k_y} (EC_e(j, t) - EC_{ethreshold}) \quad (6)$$

226 where k_y is the factor that affects the yield, EC_e is the electrical conductivity of the soil
227 saturation extract (ms cm^{-1}), $EC_{ethreshold}$ is the calibrated threshold of the electrical
228 conductivity of the soil saturation extract when the crop yield becomes affected by salt
229 (ms cm^{-1}), and B is the calibrated crop specific parameter that describes the decrease rate
230 of crop yield when EC_e increases per unit below the threshold. The electrical
231 conductivity of the soil saturation extract can be calculated as (Rhoades et al., 1989):

$$232 \quad EC_e = 1.33 + 5.88 \times EC_{1:5} \quad (7)$$

233 where $EC_{1:5}$ is the electrical conductivity of the soil extract that soil samples mixed with
234 distilled water in a proportion of 1:5.

235 *2.3.2 VADOSE Module*

236 *2.3.2.1 Moisture content at field capacity*

237 Field capacity with a shallow groundwater is different than in soils with deep
238 groundwater where water stops moving when the hydraulic conductivity becomes
239 limiting at -33 kPa. When the groundwater is shallow, the hydraulic conductivity is not
240 limiting and the water stops moving when the hydraulic potential is constant and thus
241 the matric potential is equal to the height above the water table (Gardner 1958; Gardner
242 et al., 1970a, b; Steenhuis et al. 1988; Liu et al., 2019). Assuming a unique relationship
243 between moisture content and matric potential (i.e. soil characteristic curve), the moisture



244 content at any point above the water table is a unique function of the water table depth.
245 Thus, any water added above field capacity will drain downward. When the groundwater
246 is recharged, the water table will rise and increase the moisture contents at field capacity
247 throughout the profile.

248 The moisture contents at field capacity were found by Liu et al. (2019) using the
249 simplified Brooks and Corey soil characteristic curve (Brooks and Corey, 1964)

$$250 \quad \theta = \theta_s \left[\frac{\varphi_m}{\varphi_b} \right]^{-\lambda} \quad \text{for } |\varphi_m| > |\varphi_b| \quad (8a)$$

$$251 \quad \theta = \theta_s \quad \text{for } |\varphi_m| \leq |\varphi_b| \quad (8b)$$

252 in which θ is the soil moisture content ($\text{cm}^3 \text{ cm}^{-3}$), θ_s is the saturated moisture content
253 ($\text{cm}^3 \text{ cm}^{-3}$), φ_b is the bubbling pressure (cm), φ_m is matric potential (cm), and λ is the
254 pore size distribution index. The moisture content at field capacity, $\theta_{fc}(z, h)$, for any
255 point, z , from the surface water for a groundwater at depth, h , can be expressed as (Liu et
256 al. 2019)

$$257 \quad \theta_{fc}(z, h) = \theta_s(z) \left[\frac{h-z}{\varphi_b} \right]^{-\lambda} \quad \text{for } |h-z| > |\varphi_b(z)| \quad (9a)$$

$$258 \quad \theta_{fc}(z, h) = \theta_s(z) \quad \text{for } |h-z| \leq |\varphi_b(z)| \quad (9b)$$

259 where h is the depth of the groundwater and z (cm) is the depth of the point below the
260 soil surface. Thus $(h-z)$ is the height above the groundwater and this is equal to the
261 matric potential for soil moisture content at field capacity.

262 For shallow groundwater, the matric potential at the surface is -33kPa when the
263 groundwater is 3.3 m depth. For this matric potential, as mentioned above, the
264 conductivity becomes limiting. This depth of the groundwater is therefore the lower limit
265 over which the VADOSE module is valid.



266 Evapotranspiration can lower the soil moisture content below field capacity. Thus,
267 the maximum moisture content in the VADOSE module is determined by the soil
268 characteristic curve and the height of the groundwater table, and the minimum is the
269 wilting point that can be obtained by evapotranspiration by the crop. Note that the
270 saturated hydraulic conductivity does not play a role in determining the moisture content
271 because inherently it is assumed that it is not limiting in the distribution of the water.

272 2.3.2.2 Drainable porosity

273 The drainable porosity that is a function of the depth is calculated first because it is
274 independent of time. The drainable porosity is obtained by calculating the field capacity,
275 $W_{fc}(h)$ (cm) for each layer at all groundwater depths. The total water content at field
276 capacity of the soil profile over a prescribed depth with a water table at depth h can be
277 expressed as:

$$278 \quad W_{fc}(h) = \sum_{j=1}^n [L(j) \theta_{fc}(j, h)] \quad (10)$$

279 where $\theta_{fc}(j, h)$ is the average moisture content at field capacity of layer j that can be
280 found by integrating Eq. 8 from the upper to the lower boundary of the layer and
281 dividing by the length $L(j)$ which is the height of layer j . The matric potential at the
282 boundary is equal to the height above the water table. The drainable porosity, $\mu(h)$,
283 which is a function of the groundwater depth h , can simply be found as the difference in
284 water content when the water table is lowered over a distance of $2\Delta h$.

$$285 \quad \mu(h) = \frac{W_{fc}(h + \Delta h) - W_{fc}(h - \Delta h)}{2\Delta h} \quad (11)$$

286 where $\Delta h = 0.5L(j)$.



287 2.3.2.3 Downward flux (at times of irrigation and/or precipitation)

288 **Water**

289 A downward flux occurs when either the precipitation or irrigation is greater than the
290 actual evapotranspiration. In this case, upward flux will not occur because the actual
291 evapotranspiration is subtracted from the input at the surface. We consider two cases
292 when the groundwater is being recharged and when it is not.

293 When the net flux at the surface (irrigation plus rainfall minus actual
294 evapotranspiration) is greater than that needed to bring the soil up to equilibrium
295 moisture content, the groundwater will be recharged and the distance of the
296 groundwater to soil surface decreases and the moisture content will be equal to the
297 moisture at field capacity. The fluxes from one layer to the next can be calculated simply
298 by summing the amount of water needed to fill up each layer below to the new moisture
299 content at field capacity. Hence, the percolation to groundwater, $R_{gw}(t)$, can be
300 expressed as:

301
$$R_{gw}(t) = P(t) + I(t) - E_a(t) - T_a(t) - \sum_{j=1}^n \frac{[\theta_{fc}(j, h) - \theta(j, t - \Delta t)]L(j)}{\Delta t} \quad (12)$$

302 where n is the total number of layers, $\theta(j, t)$ is the average soil moisture content in day
303 t of layer j , $E_a(t)$ is the actual evaporation, $T_a(t)$ is the actual transpiration, $P(t)$ is
304 the precipitation, and $I(t)$ is the irrigation.

305 When the groundwater is not recharged, the rainfall and the irrigation are added to
306 uppermost soil layer and when the soil moisture content will be brought up to the field
307 capacity and the excess water will infiltrate to next soil layer bringing it up to field



308 capacity. This process continues until all the rainwater is distributed. Formally the soil
 309 moisture can be expressed as

$$310 \quad \theta(j, t) = \min \left[\theta_{fc}(j, h), \left[\theta(j, t - \Delta t) + \frac{R_w(j-1, t) \Delta t}{L(j)} \right] \right] \quad (13)$$

311 where $\theta(j, t)$ is the average soil moisture content in day t of layer j , $R_w(j - 1, t)$ is the
 312 percolation rate to layer j and can be found with Eq 12 by replacing $j-1$ for n in the
 313 summation sign.

$$314 \quad R_w(j - 1, t) = P(t) + I(t) - E_a(t) - T_a(t) - \sum_1^{j-1} \frac{[\theta_{fc}(j, h) - \theta(j, t - \Delta t)]L(j)}{\Delta t} \quad (14)$$

315 For the uppermost soil layer, the water percolation can be expressed as

$$316 \quad R_w(0, t) = I(t) + P(t) - E_a(t) - T_a(t) \quad (15)$$

317 Salinity

318 The salt concentration for layer j can be expressed by a simple mass balance as:

$$319 \quad C(j, t) = \frac{\theta(j, t - \Delta t) C(j, t - \Delta t)L(j) + [R_w(j - 1, t) C(j - 1, t) - R_w(j, t) C(j, t)] \Delta t}{\theta(j, t)L(j)} \quad (16)$$

320 where $C(j, t)$ is the salt concentration of layer j at time t (g L^{-1}). The equation can be
 321 rewritten as an explicit function of $C(j, t)$

$$322 \quad C(j, t) = \left[\frac{\theta(j, t)L(j)}{1 + R_w(j, t) \Delta t} \right] \left[\frac{\theta(j, t - \Delta t) C(j, t - \Delta t)L(j) + R_w(j - 1, t) C(j - 1, t) \Delta t}{\theta(j, t)L(j)} \right] \quad (17)$$

323 For the surface layer $j=1$, we obtain

$$324 \quad C(1, t) = \left[\frac{\theta(1, t)L(1)}{1 + R_w(1, t) \Delta t} \right] \left[\frac{\theta(1, t)L(1)}{1 + R_w(1, t) \Delta t} \frac{\theta(j, t - \Delta t) C(j, t - \Delta t)L(j) + I(t) C_I \Delta t}{\theta(j, t)L(j)} \right] \quad (18)$$

325 where $C_I \Delta t$ is the salt concentration in the irrigation water.

326 The salt concentration of the groundwater $C_{gw}(t)$ can be estimated as:

$$327 \quad C_{gw}(t) = \frac{[G(t - 1) \times C_{gw}(t - 1) + C(5, t) \times R_w(t)]}{G(t - 1) + R_w(t)} \quad (19)$$



328 Where $C(5, t)$ is the soil salinity concentration of the soil layer 5 on day t (g L^{-1}),
329 $G(t - 1)$ is the difference of the groundwater depth and the depth that the largest
330 groundwater table fluctuations depth of groundwater table on day $(t-1)$ (m) (Xue et al.,
331 2018), $C_{gw}(t)$ is the soluble salt concentration of groundwater at day t (g L^{-1}).

332 2.3.2.4 Upward flux

333 For the upward flux period, it is assumed there is no downward water flux to
334 groundwater in this study. The evapotranspiration leads to the decrease of soil moisture
335 content in the vadose zone and lowers the groundwater table due to the upward
336 movement of groundwater to crop root zone and soil surface. The soil moisture content
337 is calculated by taking the difference of equilibrium moisture content associated with the
338 change of groundwater depth.

339 **Water**

340 The groundwater upward flux, $U_{gw}(h, t)$, is limited by either the maximum upward flux
341 of groundwater, $U_{gw,max}(h)$, or the actual evapotranspiration, formally stated as:

$$342 \quad U_{gw}(h, t) = \min \left[[E_a(t) + T_a(t)], U_{gw,max}(h) \right] \quad (20)$$

$$343 \quad E_a(t) = \sum_{j=1}^n E_a(j, t) \quad (21)$$

$$344 \quad T_a(t) = \sum_{j=1}^n T_a(j, t) \quad (22)$$

345 The maximum upward flux can be expressed as (Liu et al., 2019; Gardner et al., 1958)

$$346 \quad U_{gw,max}(h) = \frac{a}{e^{bh} - 1} \quad \text{for } U_{gw}^h \leq ET_p \quad (23)$$

347 where a and b are constants that need to be calibrated.

348 Two cases are considered for determining the moisture contents of the layers



349 depending on whether the actual evapotranspiration is greater or less than the maximum
350 upward flux.

351 Case I: $U_{gw,max}(h) > E_a(t) + T_a(t)$

352 In this case, where the maximum upward flux is greater than the evaporative demand, the
353 groundwater depth is updated

$$354 \quad h(t) = h(t - \Delta t) + \frac{E_a(t) + T_a(t)}{\mu(\bar{h})} \quad (24)$$

355 where $\mu(\bar{h})$ is the average drainable porosity over the change in groundwater depth h .

356 The moisture content after the change in groundwater depth becomes

$$357 \quad \theta(j, t) = \theta(j, t - \Delta t) + \theta_{fc}(j, h(t)) - \theta_{fc}(j, h(t - \Delta t)) \quad (25)$$

358 Note that when the layer is at field capacity and the upward flux is equal to the
359 evaporative flux, the layer remains at field capacity for the updated groundwater depth at
360 time t .

361 Case II: $U_{gw,max}(h) \leq E_a(t) + T_a(t)$

362 In this case, the groundwater depth is updated

$$363 \quad h(t) = h(t - \Delta t) + \frac{U_{gw,max}(h)}{\mu(\bar{h})} \quad (26)$$

364 When the upward flux is less than the sum of the actual evaporation and transpiration,
365 the moisture content is updated with the difference between the two fluxes,
366 $U_{gw,max}(h)$ and $[E_a(t) + T_a(t)]$, according to a predetermined distribution extraction of
367 water out of the root zone

$$368 \quad \theta(j, t) = \theta(j, t - \Delta t) + \theta_{fc}(j, h(t)) - \theta_{fc}(j, h(t - \Delta t)) - \frac{r(j)[E_a(t) + T_a(t) - U_{gw,max}(h)]}{L(j)} \quad (27)$$

369 The upward flux of water can be found by summing the differences in moisture content



370 above the layer j similar to Eq 14, but starting the summation at the groundwater.

371 Salinity

372 The salt from groundwater is added to the soil layers according to the root function. The
373 soil salinity concentration in layer j at day t can be expressed as

$$374 \quad C(j, t) = \frac{\theta(j, t - \Delta t) C(j, t - \Delta t)L(j) + r(j, t)U_g(h, t)C_{gw}(t)}{\theta(j, t - \Delta t)L(j) + (\theta_{fc}(j, h(t)) - \theta_{fc}(j, h(t - \Delta t)))L(j) - r(j, t)(E_a(t) + T_a(t) - U_{gw, max}(h))} \quad (28)$$

375 Since water is extracted from the reservoir that has the same concentration as in the
376 reservoir, the concentration will not change, hence the equation used to estimate the
377 groundwater salt concentration can be expressed as

$$378 \quad C_{gw}(t) = C_{gw}(t - \Delta t) \quad (29)$$

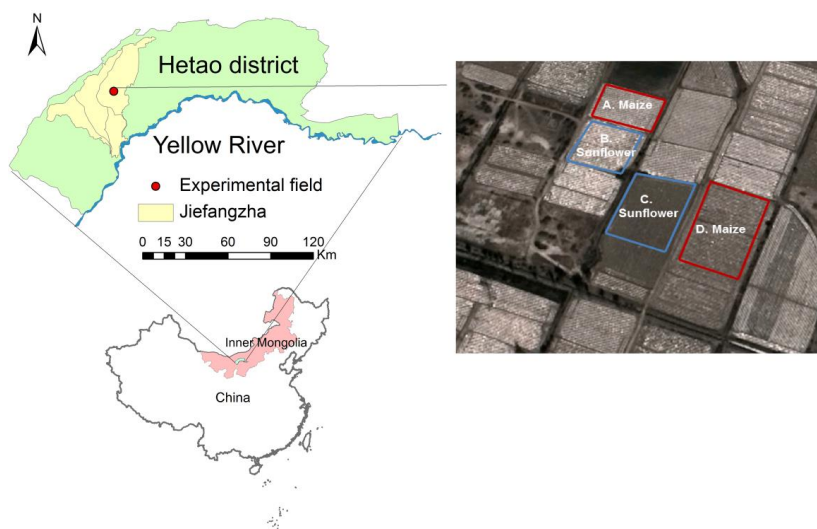
379 3. Data collection

380 3.1 Study area

381 Field experiments were conducted in 2017 and 2018 in Shahaoqu experimental station
382 in Jiefangzha sub-district, Heato irrigation district in Inner Mongolia, China (Fig. 3).
383 Irrigation water originates from the Yellow River. The area has an arid continental climate.
384 Mean annual precipitation is 155 mm a⁻¹ of which 70% falls from June to September. Pan
385 evaporation is 2000 mm a⁻¹ (Xu et al., 2010). The mean annual temperature is 7°C. The
386 soils begin to freeze in the middle of November and to thaw in end of April or beginning
387 of May. Maize, wheat and sunflower are the main crops in Jiefangzha sub-district and are
388 grown with flood irrigation. The groundwater depth is between 0.5-3 m. Regional
389 exchange of groundwater is minimal due to low gradient of 0.01-0.025 (Xu et al., 2010).
390 Thus, the groundwater mainly moves in a vertical direction in the regional scale. Soil



391 salinity in the aquifer in over 86% of the Hetao district is less than 2 g L^{-1} .



392

393 Fig. 3 Location of the Shahaoqu experimental field (Note: The figure about the layout of
394 the experimental fields is download from © Google earth)

395

396 3.2 Field observations and data

397 The layout of the experimental fields is shown in Figure 3. The areas of fields A, B, C
398 and D are 920, 2213, 1167, 1906 m^2 , respectively. Field A and D were planted with
399 maize on May 10 and harvested on September 30, 2017. In 2018, fields A and D were
400 planted with gourds and were therefore not monitored in 2018. Fields B and C were
401 seeded with sunflower in both 2017 and 2018. The sunflower was planted on June 1,
402 2017 and June 5, 2018. Harvest was on September 15 in both years. The fields were
403 flood irrigated ranging from two to five times during the growing season (Table 1). A well
404 was installed in each experimental field to monitor the groundwater depth.

405



406

407 Table 1 Irrigation scheduling for the Shahaoqu experimental fields in 2017 and 2018

Field	Year	Irrigation events	Date	Irrigation depth (mm)
A (maize)	2017	1	5/30	100
		2	6/25	162
		3	7/14	275
		4	8/6	199
	2017	1	6/26	140
		2	7/23	121
B (sunflower)	2018	1	6/20	134
		2	6/24	60
		3	7/15	114
		4	7/22	40
		5	8/31	130
C (sunflower)	2017	1	6/19	80
		2	6/30	80
	2018	1	6/20	140
		2	7/14	100
D (maize)	2017	1	6/13	150
		2	6/26	94
		3	7/6	50
		4	7/14	174
		5	8/6	120

408

409 Daily meteorological data, including air temperature, precipitation, relative humidity,
 410 wind speed, and sunshine duration, originated from the weather station at the Shahaoqu
 411 experimental station. The soil moisture content for the four experimental fields in 2017
 412 and for field C in 2018 during the crop growing season was measured every 7-10 days
 413 at the depths of 0-20, 20-40, 40-60, 60-80, 80-100 cm by taking soil samples and
 414 oven drying. For field B in 2018, the soil moisture content was monitored daily in the top
 415 100cm at 20 cm intervals using Hydra Probe Soil Sensors (Stevens Water Monitoring



416 System Inc., Portland, OR, USA). In 2017, the groundwater depths were manually
417 measured in all four experimental fields about every 7-10 days. In 2018, the
418 groundwater depth in fields B and C was recorded at 30 min intervals using an HOBO
419 Water Level Logger-U20 (Onset, Cape Cod, MA, USA). The sensors of the soil moisture
420 content and groundwater depth were connected to data loggers and downloaded via
421 wireless transmission. The crop leaf area and crop height were manually measured every
422 7-12 days.

423 Undisturbed soil samples were collected in 5 cm high rings with a diameter of 5.5
424 cm from the five soil layers where the soil moisture were taken and used for textual
425 analysis, saturated soil moisture content, field capacity and soil bulk density. The soil
426 texture was analyzed with a laser particle size analyzer (Mastersizer 2000, Malvern
427 Instruments Ltd., United Kingdom). The American soil texture classification method was
428 used in this study. Finally, the soil samples were collected 7-10 days apart to monitor the
429 change of electrical conductivity (EC). The soil samples were mixed with distilled water in
430 a proportion of 1:5 to measure the electrical conductivity of the soil water by a portable
431 conductivity meter. It is assumed that 1 ms cm^{-1} corresponds to 640 mg L^{-1} of total
432 dissolved salts (Wallender and Tanji, 2011; Xue et al., 2018).

433 3.3 Model calibration and validation

434 The observed soil moisture contents, groundwater depths, crop heights, LAIs and salinity
435 concentrations for field A with maize and sunflower fields B and C in 2017 were used for
436 calibration and the sunflower data of fields B and C in 2018 and the maize data in field
437 D in 2017 were used for validation. The initial $\vartheta_{0.33}$ was based on the measured data



438 (Table 2). The initial values of ϑ_s and ϑ_{15} were derived from the soil texture with the
439 method of Ren et al. (2016) (Table2). The default values of EPIC for sunflower and maize
440 were used as initial values for simulating crop growth (K_{cmax} and LAI_{mx} in Eq. S3, K_b in Eq.
441 S4, H_{mx} in Eq. S7, PHU in Eq. S9, T_b in Eq. S10, ad in Eq. S12, T_o and T_b in Eq. 16, RD_{mx} in
442 Eq. S18). The initial value maximum crop coefficient (K_{cmax}) in Eq. S3 in Supplementary S1
443 for evapotranspiration calculation was taken from *Sau et al.*, (2004). The initial values of
444 two groundwater parameters (a and b in Eq. 23) were based on Liu et al., (2019). The
445 Brooks and Corey soil moisture characteristic parameters (φ_b , λ in Eq. 8) were obtained
446 by fitting the outer envelope of the measure moisture content and water table data.

447 Statistical indicators were used to evaluate goodness of fit of the hydrological model
448 for both calibration and validation (Ritter and Muñoz-Carpena, 2013). The statistical
449 indicators included the root mean square error (RMSE) (Abrahart and See, 2000),

450

$$RMSE = \sqrt{\frac{1}{N} \sum_{i=1}^N (P_i - O_i)^2} \quad (30)$$

451 the mean relative error (MRE) (Dawson et al., 2006; Nash and Suscliff, 1970),

452

$$MRE = \frac{1}{N} \sum_{i=1}^N \frac{(P_i - O_i)}{O_i} \times 100\% \quad (31)$$

453 the Nash-Sutcliffe efficiency coefficient (NSE) (Nash and Suscliff, 1970),

454

$$NSE = 1 - \frac{\sum_{i=1}^N (P_i - O_i)^2}{\sum_{i=1}^N (O_i - \bar{O})^2} \quad (32)$$

455 and the determination coefficient (R^2) and regression coefficient (b) (Xu et al., 2015)

456

$$R^2 = \left[\frac{\sum_{i=1}^N (O_i - \bar{O})(P_i - \bar{P})}{[\sum_{i=1}^N (O_i - \bar{O})]^{0.5} [\sum_{i=1}^N (P_i - \bar{P})]^{0.5}} \right]^2 \quad (33)$$



457
$$b = \frac{\sum_{i=1}^N O_i \times P_i}{\sum_{i=1}^N O_i^2} \quad (34)$$

458 where N is the total number of observations; P_i and O_i are the i^{th} model predicted and
459 observed values ($i=1,2,3\dots N$), respectively; \bar{O} and \bar{P} are the mean observed values and
460 predicted values, respectively. The value of RMSE and MRE close to 0 indicates good
461 model performance. The value of NSE ranges from $-\infty$ to 1. NSE=1 means a perfect fit
462 while the negative NSE value indicates the mean observed value is a better predictor
463 than the simulated value (Moriasi et al., 2007). For b and R^2 , the value closest to 1
464 indicates good model predictions.

465 3.4 Parameters sensitivity analysis

466 A sensitivity analysis was performed to determine how the input parameters
467 affected output of the models (Cloke et al., 2008; Cuo et al., 2011). Each parameter was
468 varied over a range of -30% to 30% to derive the corresponding impact on the model
469 output. The change in output values was plotted against the change in input values.

470

471 4 Results

472 The 2017 and 2018 experimental data of the Shahaoqu farmers' fields in the Hetao
473 irrigation district (Fig.3) are presented first, followed by the calibration and validation of
474 the CROP and VADOSE modules of EPICS model.

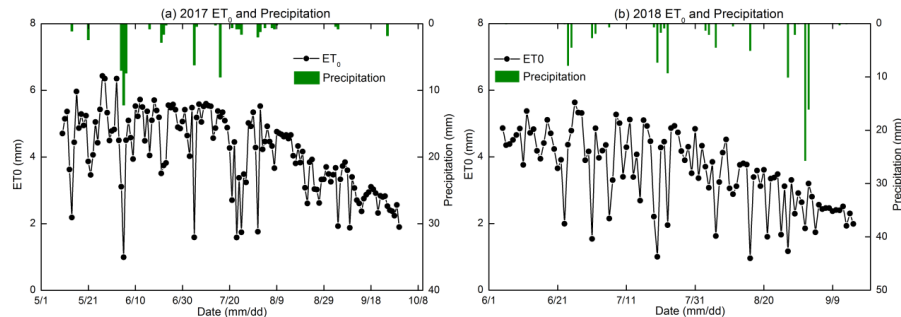
475 4.1 Results of the field experiment

476 4.1.1 Water input

477 The precipitation was 63 mm in 2017 (May 10 to September 30) and 108 mm in
478 2018 (June 1 to September 15). The precipitation from the greatest rainstorm was 26



479 mm on September 1, 2018 (Fig. 4). Irrigation provided most of the water for the crops.
480 Field A (maize) was irrigated four times with a total of 736 mm and field D (maize) was
481 irrigated five times for a total of 588 mm in 2017. Sunflower fields B and C were both
482 irrigated twice with a total water amount of 261mm and 160mm, respectively, in 2017.
483 In 2018, fields B and C were irrigated five and two times, respectively, with a total water
484 amount of 478mm and 240mm, respectively. The total reference evapotranspiration
485 from May 10 to September 30, 2017 was 595 mm and 368 mm from June 1 to
486 September 15, 2018. On a daily basis, the reference evapotranspiration ranged from 1
487 mm d⁻¹ to a maximum of 6.4 mm d⁻¹ during crop growth period (Fig. 4).



488
489 Fig 4. Reference evapotranspiration (ET₀) and precipitation during crop growth period in
490 2017 and 2018.

491

492 4.1.2 Soil physical properties

493 Based on the soil textural analysis in Table 2, the soils were classified as silt, silt loam and
494 loamy sand. Bulk densities varied from 1.24 to 1.47 Mg m⁻³ with the greatest bulk
495 densities in the 0-20 cm soil layer. There was generally more sand in the top 40 cm than
496 below. The subsoil was heavier and had the greatest percentage of silt (Table 2). The
497 moisture content at -33 kPa (0.33 bar) varied from 0.25 to 0.35 cm³cm⁻³ and at 1.5Mpa



498 (wilting point at 15 bar) ranged from 0.08 to 0.15 cm³cm⁻³ (Table 2).

499 Table 2 Soil texture and bulk density of the experimental fields in Shahaoqu

Field	Soil depth (cm)	Sand(%)	Silt(%)	Clay(%)	Soil type	ρ (Mg m ⁻³)	$\theta_{0.33}$ (m ³ m ⁻³)	θ_{15} (m ³ m ⁻³)
A	0-20cm	26	62	13	Silt loam	1.44	0.31	0.1
	20-40cm	76	22	2	Loamy sand	1.24	0.32	0.07
	40-60cm	10	79	10	Silt loam	1.33	0.33	0.12
	60-100cm	6	79	15	Silt loam	1.35	0.34	0.14
B	0-20cm	22	64	13	Silt loam	1.44	0.29	0.15
	20-40cm	16	73	11	Silt loam	1.24	0.26	0.13
	40-60cm	18	73	9	Silt loam	1.33	0.32	0.11
	60-80cm	8	77	16	Silt	1.35	0.34	0.14
	80-100cm	13	79	8	Silt loam	1.35	0.35	0.12
C	0-20cm	29	63	8	Silt loam	1.47	0.26	0.08
	20-40cm	37	56	6	Silt loam	1.33	0.25	0.08
	40-60cm	35	59	7	Silt loam	1.32	0.26	0.08
	60-80cm	14	74	12	Silt loam	1.38	0.31	0.12
	80-100cm	10	82	8	Silt	1.38	0.34	0.11
D	0-20cm	27	62	11	Silt loam	1.47	0.3	0.15
	20-40cm	5	80	15	Silt loam	1.33	0.27	0.14
	40-60cm	7	75	18	Silt loam	1.32	0.33	0.15
	60-100cm	10	81	9	Silt	1.38	0.34	0.12
						0.31	0.14	

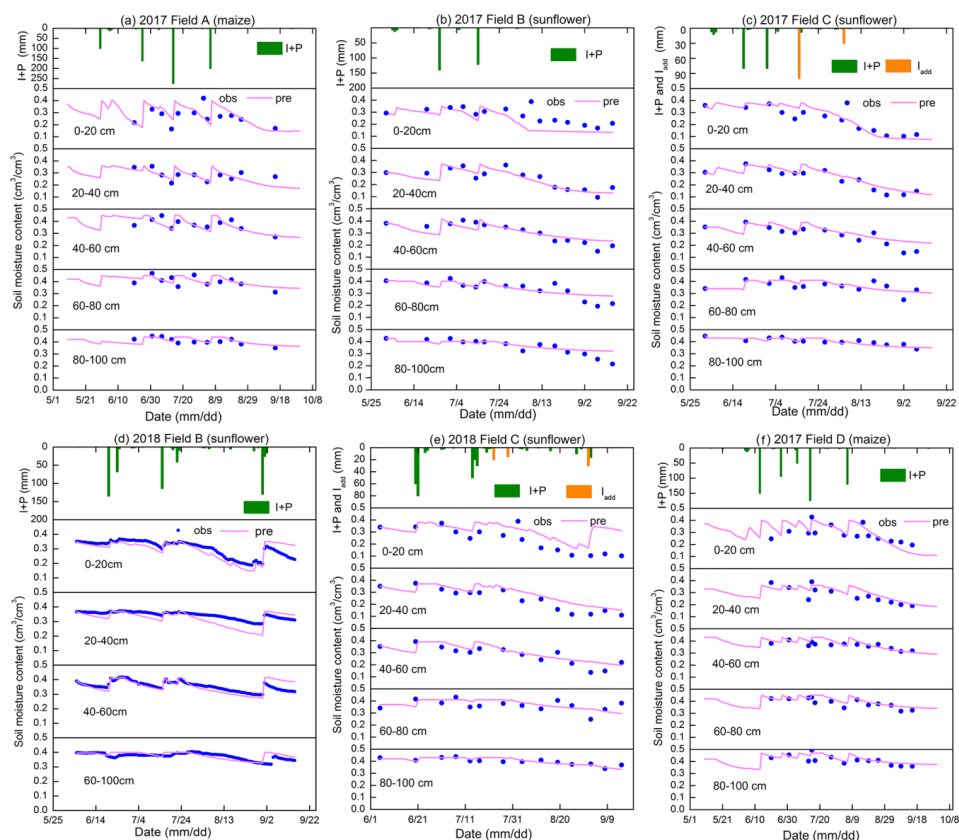
500

501 4.1.3 Soil moisture content

502 Moisture content, rainfall and irrigation amounts are depicted for the five layers and
 503 the four fields in 2017 and two fields in 2018 in Fig. 5. Blue closed spheres indicate that
 504 the moisture content was determined on cored soil samples (Figs. 5a, b, c, e, f) and
 505 close-spaced spheres when the hydra probe was used (Fig. 5d). The moisture contents
 506 were near saturation when irrigation water was added and subsequently decreased due
 507 to crop transpiration and soil evaporation (Fig. 5). In all cases, the moisture contents



508 during the main growing period remained above the moisture content at -33 kPa that
509 ranged from $0.25 \text{ cm}^3 \text{ cm}^{-3}$ to $0.34 \text{ cm}^3 \text{ cm}^{-3}$ for the 60-80 cm depth (Table 2, Fig.5). Only
510 after the last irrigation and during harvest of the crop did the moisture content in the top
511 0-40 cm for maize and 0-60 cm for sunflower decrease below the moisture content at
512 -33kPa. During the growing season, the variation of moisture content was greater in the
513 top 60 cm with the majority of the roots than in the lower depths where, after the first
514 irrigation, it remained nearly constant close to saturation.

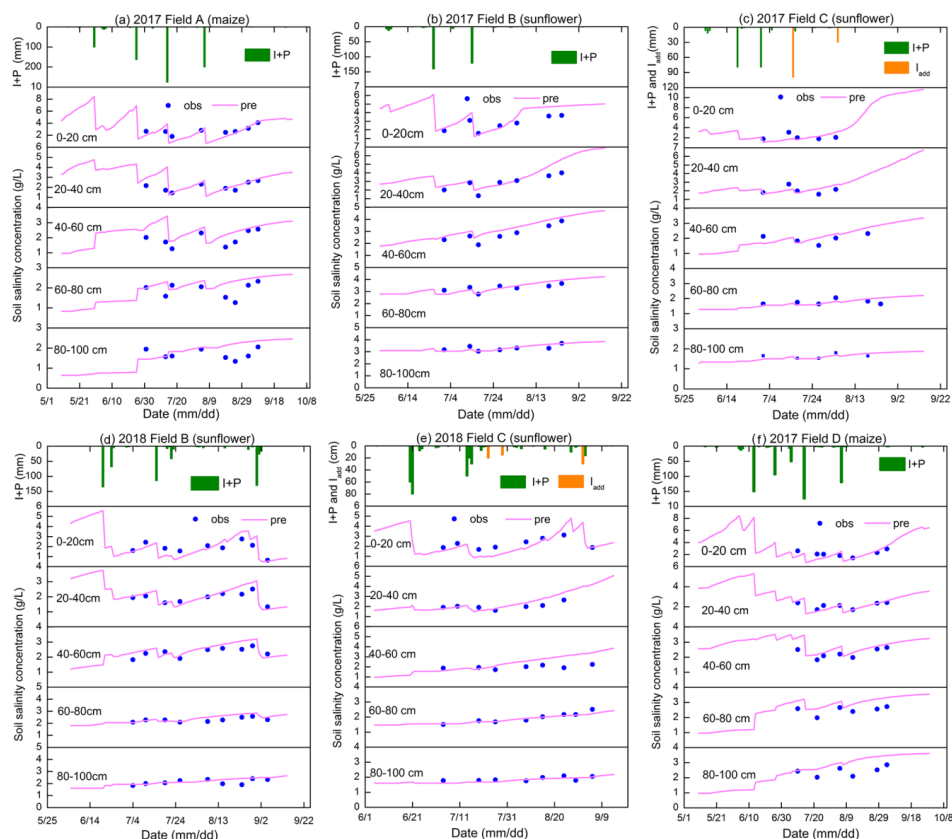


515
516 Fig. 5 Observed (blue dots) and simulated soil moisture content of the Shahaoqu
517 experimental fields during model calibration (a,b,c) and validation (d,e,f)

518



519 4.1.4 Salinity



520

521 Fig. 6 Observed (blue dots) and simulated soil salinity concentration of the experimental
522 fields in Shahaoqu during model calibration (a,b,c) and validation (d,e,f).

523

524 Overall the salt concentration is greatest at the surface and increases at all depths
525 during the growing season. Sunflower is more salt tolerant than maize and the overall
526 salt concentration was greater in the sunflower fields (Fig. 6) at comparable times of the
527 crop development for field B but not for field C. Comparing the salt concentration and
528 soil moisture patterns (Fig.5), we note that they behave similarly but opposite to each
529 other (Fig. 6). The soil salinity concentration was decreasing during an irrigation event



530 due to dilution and then gradually increasing partly due to evaporation of the water.
531 Some of the soil salt was transported to the layers below during irrigation and some salt
532 was moving upward with the evaporation from the surface. As expected, after the harvest,
533 the autumn irrigation decreased the salt concentration from fall 2017 to spring 2018.

534

535 4.1.5 Groundwater observations

536 The variation in groundwater depth during the growing season was very similar for
537 both years and in all fields. The groundwater depth for all fields was between 50 and
538 100 cm from the surface after an irrigation event and then decreased to around 150 cm
539 before the next irrigation or rainfall (Fig.7). Only after the last irrigation in August 2017
540 did the water table decrease to below 250 cm and to around 200 cm in 2018. Field D
541 followed the same pattern but the groundwater was more down from the surface. In
542 several instances, the groundwater table increased without an irrigation or rainfall event
543 in sunflower field C (Fig. 7c and 7e). This was likely related to an irrigation event either
544 from a spillover or an accidental irrigation that was not properly documented. We
545 estimated the amount of irrigation water based on the change in moisture content in the
546 soil profile (orange bars in Fig. 7c and 7e). Finally, there was a notable rise in the water
547 table of an mean 375mm “autumn irrigation” after harvest between the end of 2017
548 (Figs. 7 a, b, c) and the beginning of 2018 (Figs. 7 d, e, f), which is a common practice in
549 the Jiefangzha irrigation district to leach the salt that has accumulated in the profile
550 during the growing periods.

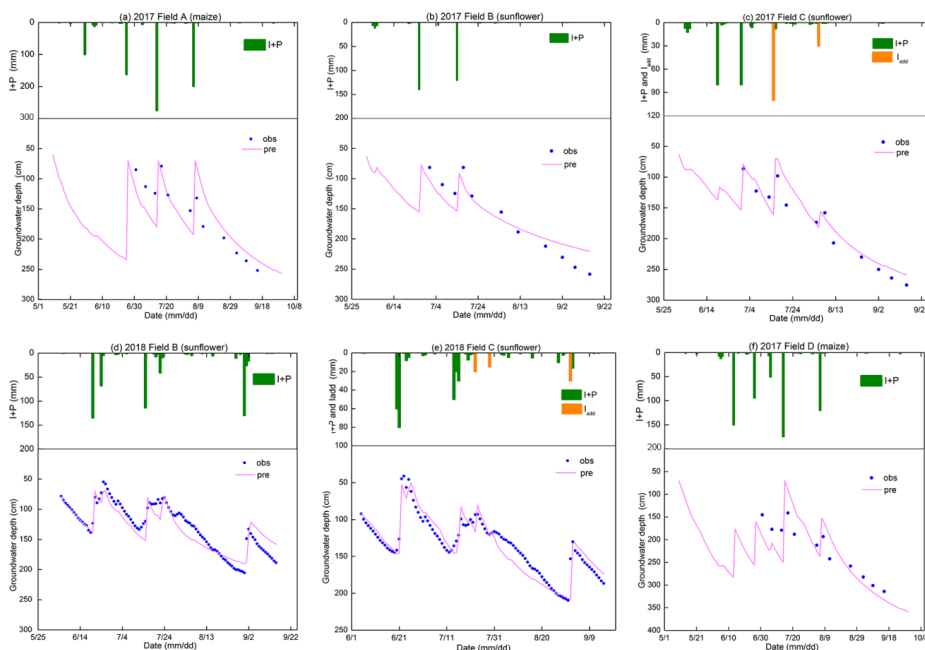
551 Note that in Fig. 7, after an irrigation event, the groundwater depth was between



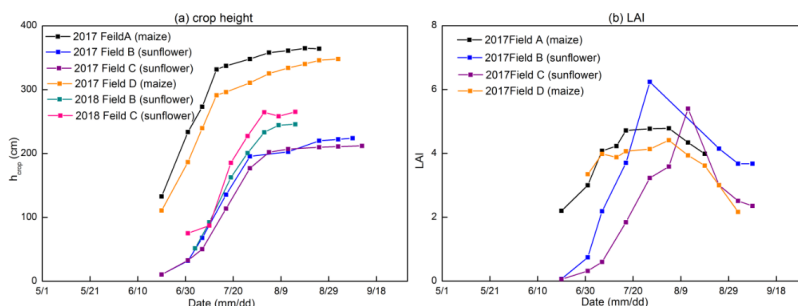
552 50-80 cm while the whole profile was saturated (Fig. 5). This is directly related to the
553 bubbling pressure of the water. After the irrigation event stopped, the water table was
554 likely at the surface but then immediately decreased because a small amount of
555 evaporated water will bring the water table down to a depth of approximately equal to
556 the bubbling pressure, φ_b , in Eq. 5. The bubbling pressures are listed in Table 3.

557 4.1.6 LAI and plant height

558 Plant height and LAI followed the typical growth curve that started slowly to rise in
559 the beginning, accelerated during the vegetative stage and then became constant during
560 the seed setting and ripening stages (Fig. 8). In the maturing stage, the leaf area index
561 decreased.



562
563 Fig. 7. Observed (blue dots) and simulated groundwater depth of the experimental fields
564 in Shahaoqu during model calibration (a, b, c) and validation (d, e, f)



565

566 Fig. 8 Observed crop height (a) and leaf area index (b) of the experimental field in
567 Shahaoqu in 2017 and 2018.

568

569 4.2 Soil Characteristic curve and drainable porosity

570 To simulate the soil moisture content and to derive drainable porosity as a function of
571 water table depth, the soil moisture characteristic curves were derived by plotting the
572 observed soil moisture content in 2017 and 2018 versus the height above the water
573 table to the soil surface for the five soil layers in Fig. 9. The Brooks-Corey equation
574 (Brooks and Corey, 1964) was fitted through outer envelope of the points. The
575 parameters of the Brooks-Corey equation were adjusted through a trial and error to
576 obtain the best fit (Table 3a). In Fig. 9, points on the left side of the soil moisture
577 characteristic curve (moisture content smaller than the field capacity) were due to water
578 removal at times when evaporative demand was greater than the upward water flux. The
579 few points at the right of the soil moisture characteristic curve indicate the soil moisture
580 was greater than field capacity and matric potential and groundwater were not yet at
581 equilibrium after an irrigation event.

582 The fitted parameter values are consistent. Field A had a greater bubbling pressure
583 and moisture content at -33 kPa than the other fields indicating that this field had more



584 clay. This was confirmed by the data in Table 2. For fields B, C and D, the bubbling
 585 pressure was greater at the 60-80 cm depth or the 80 -100 cm depth, which was also in
 586 accordance with the data in Table 2.

587 Table 3a Calibrated soil hydraulic parameters in the Brooks and Corey soil moisture
 588 characteristic curve.

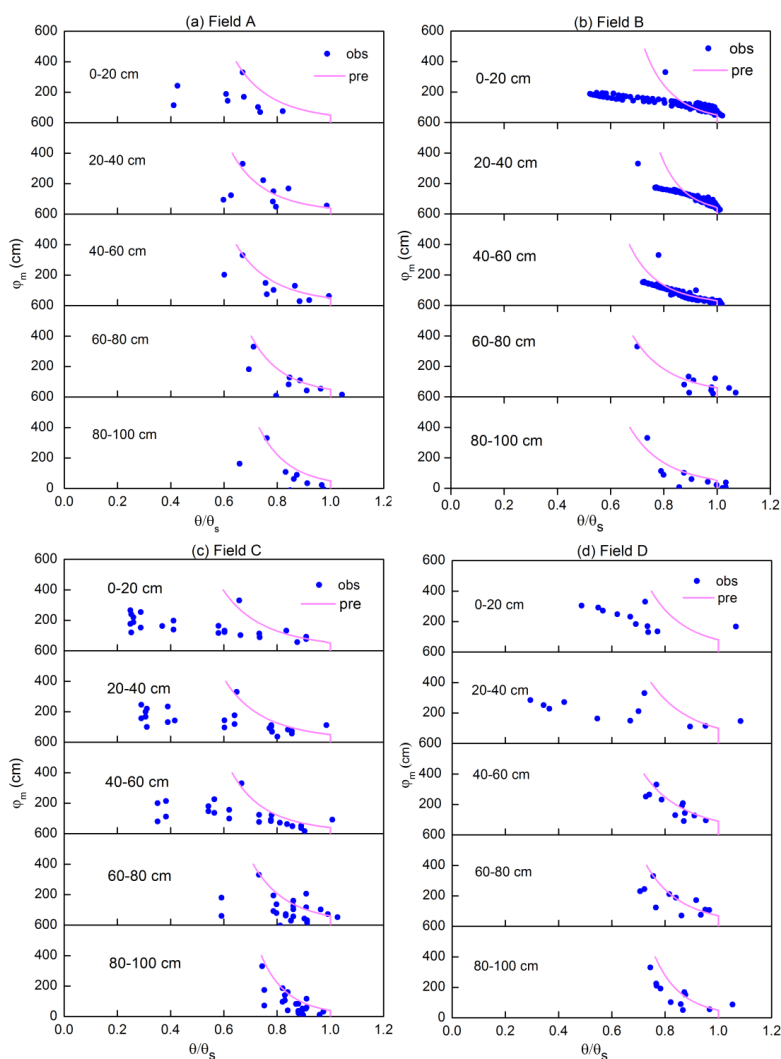
Field	Parameter	0-20cm	20-40cm	40-60cm	60-80cm	80-100cm
A	θ_s	0.4	0.36	0.43	0.45	0.47
	φ_b	80	100	90	70	50
	λ	0.18	0.21	0.22	0.18	0.15
B	θ_s	0.35	0.37	0.41	0.4	0.4
	φ_b	50	55	33	60	55
	λ	0.14	0.11	0.16	0.2	0.2
C	θ_s	0.38	0.37	0.39	0.71	0.43
	φ_b	55	50	40	60	40
	λ	0.26	0.24	0.2	0.18	0.13
D	θ_s	0.4	0.36	0.45	0.45	0.44
	φ_b	50	40	55	50	50
	λ	0.21	0.2	0.3	0.17	0.15

589 Note: θ_s is the soil moisture at saturation ($\text{cm}^3\text{cm}^{-3}$), φ_b is bubbling pressure (cm), λ is the
 590 pore size distribution index.

591 Table 3b Calibrated groundwater parameters

Field\parameters	A	B	C	D
a	70	75	110	70
b	0.02	0.025	0.022	0.015

592



593

594 Figure. 9 Soil moisture characteristic curves of five soil layers in the experimental fields.
595 The red line is the fit with the Brooks-Corey equation.

596

597 4.3 Parameters sensitivity analysis

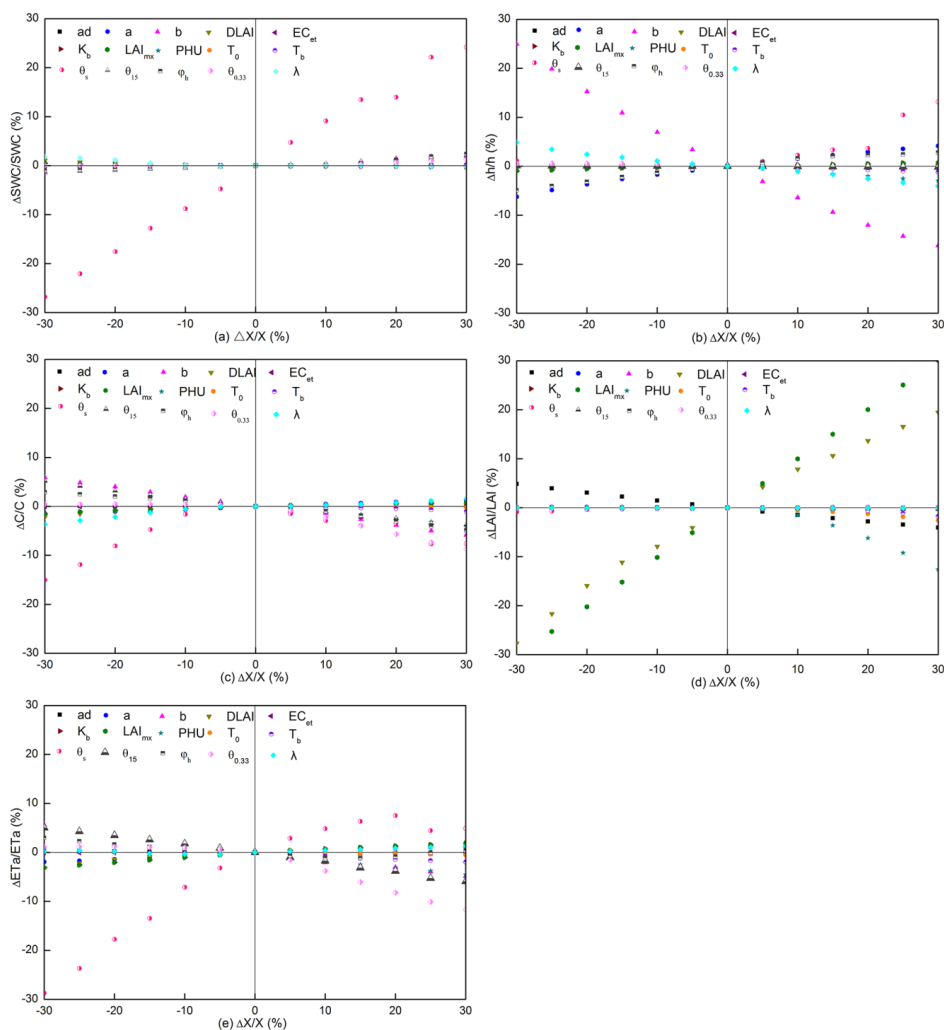
598 The results of sensitivity analysis of the 15 input parameters on 5 output parameters are
599 shown in Fig. 10. The evaluated output parameters are soil moisture content,
600 groundwater depth, soil salinity concentration, field evapotranspiration, and crop leaf



601 area index (LAI). Steeper lines indicate a greater sensitivity of the parameter.

602 The results of the sensitivity analysis show that moisture content predictions (Fig
603 10a) are the most sensitive to the input value of the saturated moisture content (θ_s).
604 None of the other parameters are very sensitive. The input parameter with the most
605 sensitivity for *groundwater depth* (Fig. 10b), is the saturated moisture content as well.
606 Other less sensitive parameters are the exponent b and constant a in Eq. 23 in predicting
607 the upward flux and the bubbling pressure, φ_b , of the soil moisture characteristic curve
608 (Eq. 8a). Likewise, in case of the *salinity* predictions (Fig. 10c), the saturated moisture
609 content gives the greatest relative change in salt content. Less sensitive, but still
610 important, are the field capacity, $\theta_{0.33}$, the bubbling pressure, φ_b , and the exponent λ of
611 the soil characteristic curve (Eq. 8a) and b in Eq. 23. The sensitive parameters for the *leaf*
612 *area index (LAI)* (Fig 10d) are the maximum potential leaf area index, LAI_{max} and fraction
613 of growing season when leaf area declines (*DLA*) followed by total potential heat units
614 required for crop maturation (*PHU*). Finally, for the evapotranspiration (Fig 10e), the
615 saturated soil moisture content is the most sensitive parameter, and other less sensitive
616 parameters are the exponent b and field capacity.

617 Thus, the model output is most sensitive to the input parameters that define the soil
618 hydraulic properties, groundwater flux and crop growth. As expected, since the soil
619 remains near field capacity, the parameters that relate to the reduction of evaporation
620 when the soil dries out are insensitive. When used in the simulation practices, the model
621 needs to be calibrated and verified to avoid high error from parameters uncertainty.



622

623 Figure. 10 Parameters sensitivity analysis for (a) soil moisture content, (b) groundwater
 624 depth, (c) salt salinity concentration, (d) LAI, (e) ET

625

626 4.4 Model calibration and validation

627 The model parameters were calibrated and validated using the observed moisture
 628 contents, groundwater depth, plant height, leaf area index and the calculated
 629 evapotranspiration. For calibration, the data collected in 2017 were used for sunflower



630 fields B and C and maize field A. Since farmers did not grow maize in 2018, the 2017
631 data of maize field D, together with sunflower fields B and C in 2018 were used for
632 validation. The optimal parameter set was determined using graphical similarity between
633 observed and predicted results together with near optimum performance of the
634 statistical indicators while keeping all values within physical acceptable ranges.

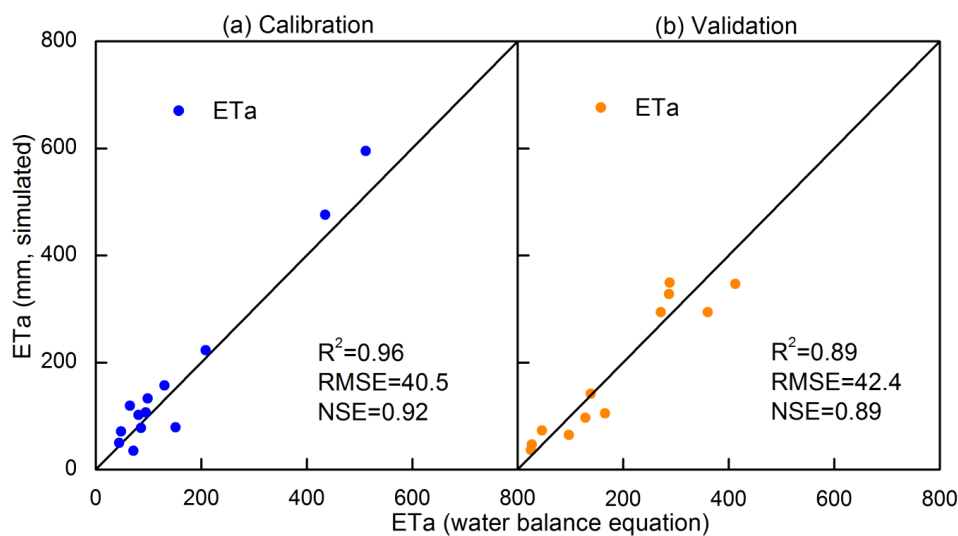
635 As a way of reducing the number of parameters that needed to be calibrated, we
636 initially selected one to three most sensitive parameters for each of the observed time
637 series, starting with evapotranspiration (including LAI and crop height) followed by
638 moisture content, groundwater depth, and salt content in the soil. This cycle was
639 repeated several times until changes became small. The last stage of the calibration
640 consisted of fine-tuning the remaining least sensitive parameters.

641 To calibrate the parameters in the CROP module, we calculated evapotranspiration
642 during the crop growth period with the observed soil moisture content and groundwater
643 depth by the soil water balance method. In addition, we used the observed LAI
644 measurements in 2017 and plant height in both 2017 and 2018. LAI was not measured
645 in 2018. The $DLAI$, LAI_{mx} and H_{mx} in the crop module were adjusted to fit the observed
646 LAI and crop height values. In addition, we fitted the $\theta_{0.33}$ moisture content to obtain a
647 good fit of the evapotranspiration. The saturated moisture content values were not
648 adjusted since they were already determined for fitting the soil characteristic curve. The
649 exponent b and constant a in Eq. 23 were adjusted to fit the observed soil moisture
650 content and groundwater depth.

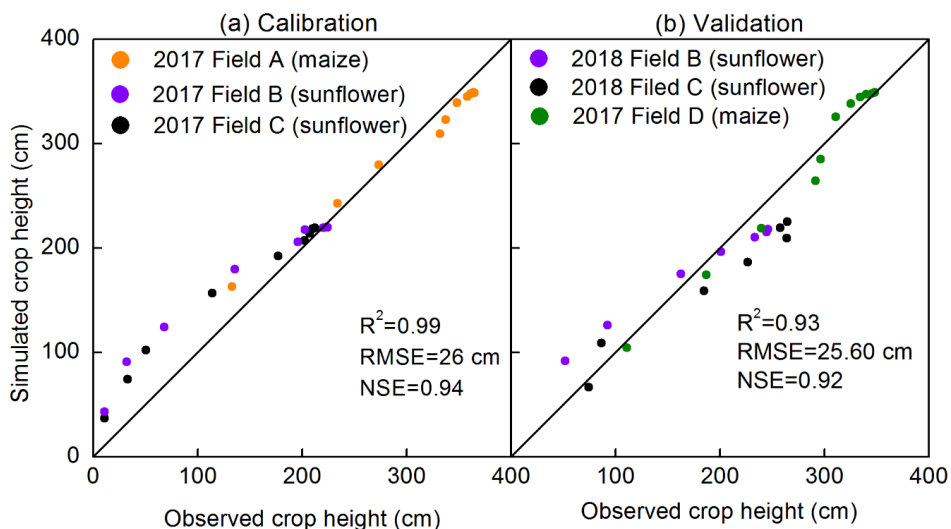
651 *4.4.1 Evapotranspiration, crop height and leaf area index*



652 The predicted evapotranspiration and that calculated from the mass balance show a
653 good agreement with Nash Sutcliff values ranging from 0.96-0.89 during calibration and
654 validation (Fig. 11 and Table 4). The calibrated predictions of plant height fitted the
655 observed values well during calibration and validation with Nash Sutcliff values ranging
656 from 0.77-0.96 for the individual fields (Table 4) and over 90% when the data was
657 pooled for the fields during calibration and validation (Fig.12). LAI was not measured in
658 2018. During calibration, Nash Sutcliff predicted LAI values were good for sunflower but
659 not as good for maize but the coefficient of determination and slope in the regression
660 were acceptable (Table 4, Fig. 13). In addition, the overall trend was predicted reasonably
661 well (Fig. 13b).

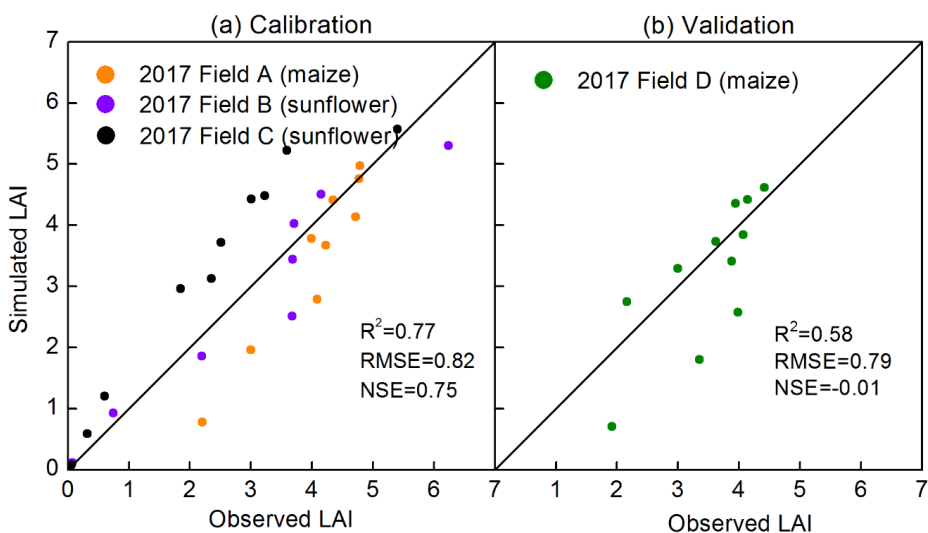


662
663 Fig. 11 Comparison of predicted and observed actual evapotranspiration: a) Calibration
664 and b) Validation



665

666 Fig.12 Comparison of predicted and observed crop height: a) Calibration and b)
 667 Validation



668

669 Fig. 13 Comparison of predicted and observed LAI: a) Calibration and b) validation

670

671

672



673 Table 4 Model error statistics for calibration and validation of model in 2017 and 2018
 674 (Mean relative error, MRE; root mean square error, RMSE; Regression slope; Coefficient of
 675 determination, R^2 ; Regression coefficient, slope).

Process	Field	Variable	MRE (%)	RMSE ($\text{cm}^3\text{cm}^{-3}\text{cm}$ or gL^{-1} or mm)	NSE	R^2	Regression coefficient slope
Calibration	2017 Field A (maize)	SWC (0-1m)	2.9	0.04	0.8	0.56	1.01
		GWD	4.5	33.8	0.64	0.64	0.97
		LAI	-17.4	0.78	0.11	0.92	0.89
		hcrop	0.04	16.2	0.95	0.99	0.97
		C	13.9	0.5	0.27	0.49	1.07
	2017 Field B (sunflower)	SWC (0-1m)	-1.2	0.04	0.71	0.74	0.97
		GWD	6.0	22.9	0.86	0.98	0.96
		LAI	4.7	0.58	0.9	0.92	0.91
		hcrop	6.8	33.5	0.83	0.96	1.1
		C	11.0	0.55	0.27	0.7	1.1
	2017 Field C (sunflower)	SWC (0-1m)	8.5	0.04	0.88	0.9	1.05
		GWD	-7.3	19.1	0.91	0.94	0.94
		LAI	48.6	1.0	0.59	0.93	1.29
		hcrop	5.42	27.4	0.88	0.98	1.07
		C	-1.6	0.52	-0.64	0.08	0.94
ETa		12.2	40.5	0.92	0.96	1.11	
Validation	2018 Field B (sunflower)	SWC (0-1m)	-2.3	0.03	0.43	0.68	0.98
		GWD	4.86	16.1	0.83	0.84	1.01
		hcrop	12.5	26.9	0.86	0.99	0.95
		C	4.0	0.35	0.18	0.72	1.06
	2018 Field C (sunflower)	SWC (0-1m)	17.3	0.06	0.64	0.72	1.04
		GWD	2.1	13.8	0.86	0.87	1.01
		hcrop	-10.3	36.4	0.77	0.97	0.84
		C	0.51	0.33	0.11	0.73	1.02
	2017 Field D (maize)	SWC (0-1m)	6.1	0.04	0.68	0.77	1.05
		GWD	0.64	39.1	0.52	0.71	1.01
LAI		-10.7	0.79	-0.02	0.58	0.93	
hcrop		-1.7	13.6	0.96	0.98	1	
C		9.8	0.51	-1.11	0.54	1.11	
ETa	8.0	42.4	0.89	0.89	0.95		

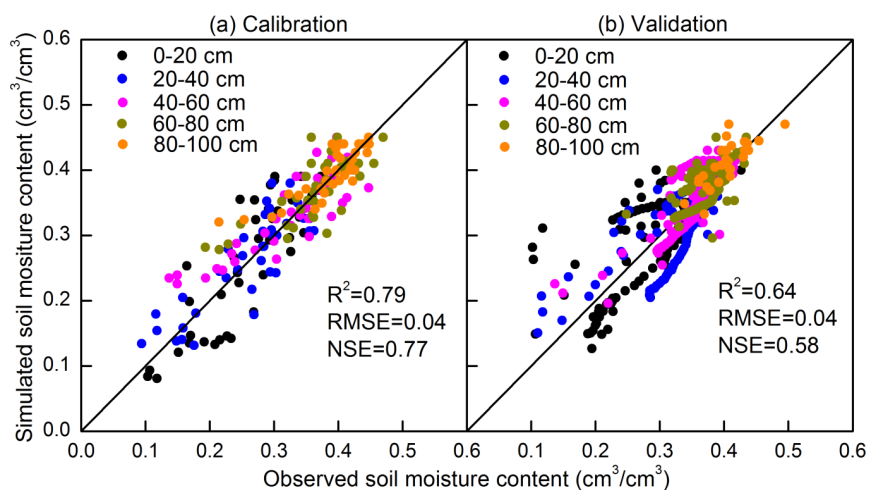
676 Note: SWC is the soil moisture content, GWD is the groundwater depth, LAI is the leaf
 677 area index, hcrop is the height of the crop, C is the soil salinity concentration, ETa is the
 678 actual evapotranspiration.



679 *4.4.2 Soil moisture and groundwater depth*

680 Next, the moisture contents and groundwater table were fitted with the parameters in the
681 Vadose model without changing the parameters in the CROP module. Saturated moisture
682 content was the most sensitive parameter for calibrating the moisture content (Fig.10a).
683 Since this value was already determined a priori from the soil characteristic curve (Table
684 3a), we could not use other parameters to obtain a better fit since none were sensitive
685 (Fig.10a). Therefore, we calibrated the groundwater parameters (i.e., a and b parameters
686 (Eq. 23)) together with the moisture content to obtain the best fit for both. The fitted a
687 and b values are listed in Table 3b. The fitted parameters between the four experimental
688 fields were similar but not the same. This can be expected in river plains where soils can
689 vary over short distances.

690 Overall, the moisture contents were predicted well during calibration and validation
691 (Figs. 5, 14 and Table 4) with the exception of field B during validation (Table 4) with a
692 NSE of 0.43. The moisture contents were predicted most accurately in the layers from
693 40-100cm where the soil moistures were at field capacity during most of the growing
694 season (Fig. 14). In the top 40 cm, the predicted soil moisture content deviated from
695 observed moisture contents, especially at the dryer end (Fig. 5 and 14). Unlike at deeper
696 depths, evapotranspiration determined the moisture contents at shallow depths.
697 Prediction of evapotranspiration introduced additional uncertainties such as the
698 distribution of the root system. This uncertainty is also likely the reason why the 2018
699 moisture contents during the validation are acceptable but not predicted as well as in
700 2017.

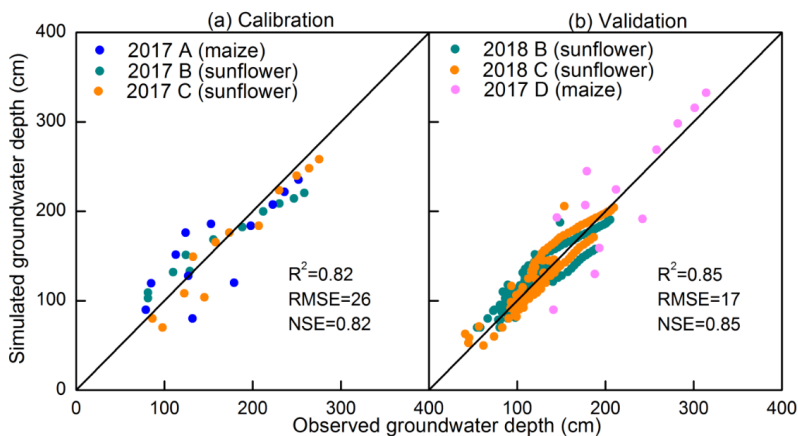


701

702 Fig. 14 Comparison of predicted and observed soil moisture content: a) calibration and b)
703 validation

704

705 The predicted and observed groundwater depths are in good agreement during both
706 calibration and validation (Figs 7, 15). The MRE values were within $\pm 10\%$ and the NSE
707 values ranged from 0.52 for field D during validation to 0.91 in field C during calibration
708 where some of the recharge events were estimated (Table 4).



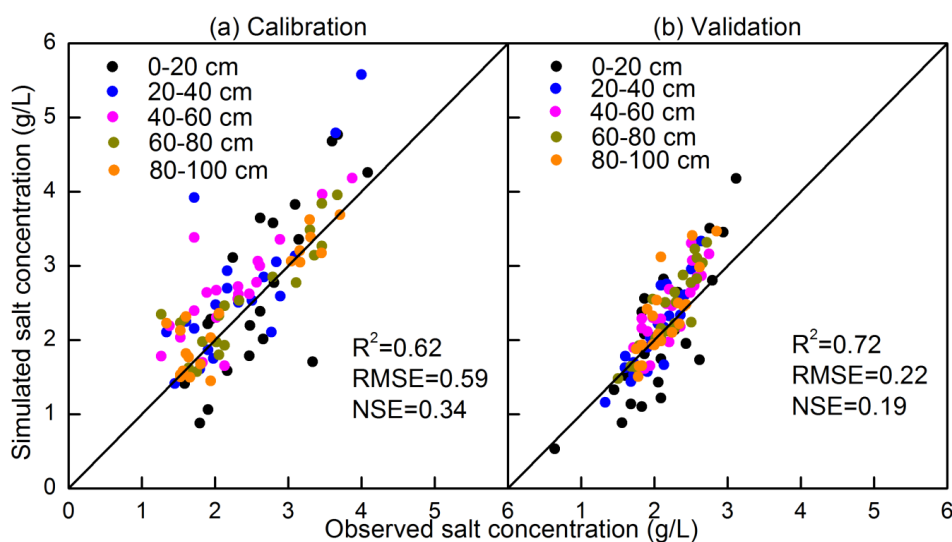
709

710 Fig. 15 Comparison of predicted and observed groundwater depth a) calibration and b)
711 validation.



712 4.4.3 *Soil salinity*

713 The only parameter that could be adjusted each year for calibration of the salt
714 concentrations was the initial salt concentration. Despite the limited calibration, the
715 observed and predicted values were in close agreement (Fig. 6, 16) with predicted salt
716 concentrations in the top layers decreasing after an irrigation event as observed. The
717 Nash Sutcliffe efficiency values were poor (Table 4), likely because the concentration
718 varied only slightly, and the mean was not predicted accurately. Similarly to the moisture
719 contents, the salt concentration in the layers below 40 cm was predicted more accurately
720 than the layers above the 40 cm. Overall, the model can predict the law of salt
721 concentration fluctuation during crop growth period and the prediction results are
722 acceptable.



723

724 Fig. 16 Comparison of predicted and observed salt concentration during calibration (a)
725 and validation (b)

726 **5. Discussion**



727 The EPICS model is a surrogate model that can be applied in areas with shallow
728 groundwater. It can simulate the soil moisture content and salt concentration for layers in
729 the soil, the groundwater depth, upward movement of water from groundwater,
730 evapotranspiration, and plant growth.

731 The model is different from traditional models that are based on Richards equation;
732 instead of calculating the fluxes first, in the EPICS model, the groundwater depth is
733 calculated first based either on the amount of water removed by evapotranspiration on
734 days without rain or irrigation or recharge to groundwater on the other days.
735 Subsequently, when the groundwater is sufficiently shallow and the potential upward flux
736 from the groundwater is greater than the evaporative demand, the moisture contents are
737 adjusted so that that soil moisture and groundwater depth are in equilibrium (i.e., field
738 capacity). In this case, the matric potential is equal to the height above the water table
739 and the moisture contents can be found with the soil characteristic curve. When the
740 upward flux is less than the evaporative demand of the atmosphere and crop, the
741 difference between the upward moisture content is determined by first decreasing the
742 moisture content below the field capacity. The flux of water in the soil is then calculated
743 based on the changes in water content. The advantage is fewer input parameters needed
744 when compared with other numerical models (Šimůnek et al., 1996; Dam et al., 1997).
745 For example, the hydraulic conductivity is not used in EPICS.

746 Although the uncertainties of field experimental observations and input data of the
747 model affected the accuracy of simulation results, EPICS compares well with other models.
748 Xu et al. (2015) tested the SWAP-EPIC for two lysimeters grown with maize on the same



749 experimental farm in the Hetao irrigation district where our experiment was carried out.
750 The SWAP model solves the Richards' Equation numerically with an implicit backward
751 scheme and is combined by Xu et al. (2015) with the EPIC model. The accuracy of our
752 simulation results, despite the difference in complexity, are very similar. The moisture
753 contents were simulated slightly better with EPICS, the groundwater depth was nearly
754 the same, and the LAI values were predicted more accurately in the SWAP-EPIC model.
755 Xue et al. (2015) did not simulate the salt content of the soil. Compared to less data and
756 computational intensive models that are applied in the Yellow River, the soil moisture
757 content were simulated more accurately by EPICS than in the North China Plain with 30
758 m deep groundwater by surrogate models of Kendy et al. (2003) and Yang et al. (2015
759 a,b) and in the Hetao irrigation district by Gao et al. (2017b) and Xue et al. (2018) during
760 the crop growth period.

761 To obtain more accurate results in the future, the upward capillary flux from
762 groundwater needs to be improved. In addition, the evapotranspiration measured
763 independently, using Eddy covariance (Zhang et al., 2012; Armstrong et al., 2008) and
764 Bowen ratio-energy balance method (Zhang et al., 2007) should be further used to test
765 performance of the model in the future study.

766 The limitation of the EPICS model is it can only be applied in areas where
767 groundwater is generally less than 3.3 m deep. When the groundwater is deeper than 3.3
768 m, the field capacity of the surface soil is determined by the moisture content when the
769 hydraulic conductivity becomes limiting and not by the depth of the groundwater.

770 Overall, the present model has the advantage that it greatly simplifies the calculation



771 of the moisture content, groundwater depth and salt content and despite that, gives
772 results similar to or better than other models applied in the Yellow river basin.

773 **6. Conclusions**

774 A novel surrogate field hydrological model called *Evaluation of the Performance of*
775 *Irrigated Crops and Soils* (EPICS) was developed for irrigated areas with shallow
776 groundwater. The model was tested with two years experimental data collected by us for
777 sunflower and one year of maize on replicated fields in the Hetao irrigation district, a
778 typical arid to semi-arid irrigation district with a shallow aquifer. The EPICS model uses
779 the soil moisture characteristic curve, upward capillary flux, and groundwater depth to
780 derive the drainable porosity and predict the soil moisture contents and salinity. The
781 evaporative flux is calculated with equations in EPIC (Environmental Policy Integrated
782 Climate) and root distribution equation.

783 The simulation results show that the EPICS model can predict the soil moisture
784 content and salt concentration in different soil layers, groundwater depth, and crop
785 growth on a daily time step with acceptable accuracy during calibration and validation.
786 The saturated soil moisture content is the most sensitive parameter for soil moisture
787 content, salt concentration, and ET in our model.

788 In the future, the model should be tested in other areas with shallow groundwater
789 that can be found in surface irrigated sites and in humid climates in river plains. Once
790 fully tested, the EPICS model can be used for optimizing water use at the local scale but,
791 more importantly, on a watershed scale in closed basins where every drop of water
792 counts.



793

794 **Data availability:** The observed data used in this study are not publicly accessible. These
795 data have been collected by personnel of the College of Water Resources and Civil
796 Engineering, China Agricultural University, with funds from various cooperative sources.
797 Anyone who would like to use these data, should contact Zhongyi Liu, Xianghao Wang
798 and Zailin Huo to obtain permission.

799 **Author contributions:** LZ and XW collected the data. ZL, ZH, CW, GH, XX and TS
800 contributed to the development of the model. The simulations with the model were done
801 by ZL, ZH and TS. Preparation and revision of the paper were done by ZL under the
802 supervision of TS and ZH.

803 **Competing interests:** The authors declare that they have no conflicts of interest.

804 **Acknowledgements:** Peggy Stevens helped greatly with polishing the English. We thank
805 Xianghao Wang and Limin Zhang and the technicians in the Shahaoqu experimental
806 station who helped in collecting data.

807 **Financial support:** This study has been supported by National Key Research and
808 Development Program of China (2017YFC0403301) and the National Natural Science
809 Foundation of China (No. 51639009, 51679236).

810

811

References

812 Abrahart, R.J and See, L.: Comparing neural network and autoregressive moving average
813 techniques for the provision of continuous river flow forecasts in two contrasting
814 catchments. *Hydro. Processes*, 14: 2157-2172. [http://doi.org/10.1002/1099-1085\(20000815/30\)14:11/12<2157::AID-HYP57>3.0.CO;2-S](http://doi.org/10.1002/1099-1085(20000815/30)14:11/12<2157::AID-HYP57>3.0.CO;2-S). 2000.



- 817 Allen, R.G., Pereira, L.S., Raes, D., and Smith, M.: Crop evapotranspiration. Guidelines
818 for computing crop water requirements-FAO Irrigation and Drainage Paper 56, FAO,
819 Rome. 1998
- 820 Armstrong, R.N., Pomeroy, J. W., Martz, L.W.: Evaluation of three evaporation estimation
821 methods in a Canadian prairie landscape. *Hydrol. Process*, 22(5): 2801-2815.
822 [https:// doi.org/ 10.1002/hyp.7054](https://doi.org/10.1002/hyp.7054). 2008.
- 823 Asher, M.J., Croke, B.F.W., Jakeman, A.J. and Peeters, L.J.M.: A review of surrogate models
824 and their application to groundwater modeling. *Water Resour Res*, 51:5957-5973.
825 <http://doi.wiley.com/10.1002/2015 WRO16967>. 2015. Blanning, R. W., The
826 construction and implementation of metamodels, *Simulation*, 24(6): 177-184.
827 [https:// doi.org/10.1177/003754977502400606](https://doi.org/10.1177/003754977502400606). 1975.
- 828 Brooks, R.H., and Corey, A.T.: Hydraulic properties of porous media, *Hydrology Paper 3*.
829 Colorado State University. Fort Collins, Colorado, 37pp, 1964.
- 830 Blanning, R.W.: Construction and Implementation of Metamodels. *Simulation*,
831 24(6):177-184. [https:// doi.org/ 10.1177/003754977502400606](https://doi.org/10.1177/003754977502400606). 1975.
- 832 Chen, C., Wang, E., and Yu, Q.: Modelling the effects of climate variability and water
833 management on crop water productivity and water balance in the North China Plain.
834 *Agr. Water Manage.*, 97:1175-1184. [https://](https://doi.org/10.1016/j.agwat.2008.11.012)
835 doi.org/10.1016/j.agwat.2008.11.012. 2010.
- 836 Chen, S., Huo, Z., Xu, X., Huang, G.: A conceptual agricultural water productivity model
837 considering under field capacity soil water redistribution applicable for arid and
838 semi-arid areas with deep groundwater, *Agr Water Manage*, 213, 309-323. [https://](https://doi.org/10.1016/j.agwat.2018.10.024)
839 doi.org/10.1016/j.agwat.2018.10.024. 2019.
- 840 Cloke, H., Pappenberger, F., Renaud, J.: Multi-Method Global Sensitivity Analysis (MMGSA)
841 for modelling floodplain hydrological processes. *Hydrol Process*, 22(1): 1660-1674.
842 [https:// doi.org/ 10.1002/hyp.6734](https://doi.org/10.1002/hyp.6734). 2008.
- 843 Cuo, L., Giambelluca, T., Ziegler, A.: Lumped parameter sensitivity analysis of a
844 distributed hydrological model within tropical and temperate catchments. *Hydrol*
845 *Process*, 25(15): 2405-2421. [http://doi.org/ 10.1002/hyp.8017](http://doi.org/10.1002/hyp.8017). 2011.
- 846 Dam, J.C. Van., Huygen, J, Wesseling, JG, Feddes, RA., Kabat, P., Walsum, PEV.
847 Van., Groenendijk, P., Diepen.: Theory of SWAP version 2.0. Simulation of water flow,
848 solute transport and plant growth in the soil-water-atmosphere-plant environment.
849 Report 71, Department Water Resources, Wageningen Agricultural University.
850 Technical document 45, DLO Winand Staring Centre, Wageningen, 152pp, 1997.



- 851 Dawson, C.W., Abrahart, R.J., Shamseldin, A.Y., Wilby, R.L.: Flood estimation at ungauged
852 sites using artificial neural networks. *J Hydrol.* 319: 391-409.
853 <http://doi.org/10.1016/j.jhydrol.2005.07.032>. 2006.
- 854 Dehaan, R., and Taylor, G.: Field-derived spectra of salinized soils and vegetation as
855 indicators of irrigation-induced soil salinization, *Remote Sens Environ.* 80(3),
856 406-417. [https:// doi.org/10.1016/S0034-4257\(01\)00321-2](https://doi.org/10.1016/S0034-4257(01)00321-2). 2002.
- 857 Delonge, K. C., Ascough, J. C., Andales, A. A., Hansen, N. C., Garcia, L. A., Arabi, M.:
858 Improving evapotranspiration simulations in the CERES-Maize model under limited
859 irrigation. *Agr Water Manage.* 115: 92-103. [http://doi.org/](http://doi.org/10.1016/j.agwat.2012.08.013)
860 [10.1016/j.agwat.2012.08.013](http://doi.org/10.1016/j.agwat.2012.08.013). 2012.
- 861 Doherty, J. and Simmons C.: Groundwater modelling in decision support: reflections on a
862 unified conceptual framework, *Hydrogeol. J.* 21(7), 1531-1537. [https://](https://doi.org/10.1007/s10040-013-1027-7)
863 doi.org/10.1007/s10040-013-1027-7. 2013.
- 864 Feng, Z., Wang, X., Feng, Z.: Soil N and salinity leaching after the autumn irrigation and
865 its impact on groundwater in Hetao Irrigation District, China. *Agr Water Manage.*
866 71(2): 131-143. [https:// doi.org/10.1016/j.agwat.2004.07.001](https://doi.org/10.1016/j.agwat.2004.07.001). 2005.
- 867 Flint, A.L., Flint, L.E., Kwicklis, E.M., Fabryka-Martin, J.T., and Bodvarsson, G.S.: Estimating
868 recharge at Yucca Mountain, Nevada, USA: comparison of methods. *Hydrogeol. J.*,
869 10:180-204. [https:// doi.org/ 10.1007/s10040-001-0169-1](https://doi.org/10.1007/s10040-001-0169-1). 2002.
- 870 Gao, X., Huo, Z., Bai, Y., Feng, S., Huang, G., Shi, H., and Qu, Z.: Soil salt and groundwater
871 change in flood irrigation field and uncultivated land: a case study based on 4-year
872 field observations. *Environ. Earth Sci.*, 73:2127-2139. [https://](https://doi.org/10.1007/s12665-014-3563-4)
873 doi.org/10.1007/s12665-014-3563-4. 2015.
- 874 Gao, X., Huo, Z., Qu, Z., Xu, X., Huang, G., and Steenhuis, T.S.: Modeling contribution of
875 shallow groundwater to evapotranspiration and yield of maize in an arid area. *Sci.*
876 *Rep-UK* 7. [https:// doi.org/10.1038/srep43122](https://doi.org/10.1038/srep43122). 2017.
- 877 Gardner, W.: Some study-state solutions of the unsaturated moisture flow equation with
878 application to evaporation from a water table. *Soil Sci.*, 85:228-232. 1958.
- 879 Gardner, W., Hillel, D., and Benyamini, Y.: Post-Irrigation Movement Soil Water 1.
880 Redistribution. *Water Resour Res.*, 6:851-860. [https:// doi.org/](https://doi.org/10.1029/WR006i003p00851)
881 [10.1029/WR006i003p00851](https://doi.org/10.1029/WR006i003p00851). 1970a.



- 882 Gardner, W., Hillel, D., and Benyamini, Y.: Post-Irrigation Movement of Soil Water 2.
883 Simultaneous Redistribution and Evaporation. *Water Resour Res.*, 6:1148-1153.
884 [https:// doi.org/ 10.1029/WR006i004p01148](https://doi.org/10.1029/WR006i004p01148). 1970b.
- 885 Guo, S., Ruan, B., Chen, H., Guan, X., Wang, S., Xu, N. and Li, Y.: Characterizing the
886 spatiotemporal evolution of soil salinization in Hetao Irrigation District (China) using
887 a remote sensing approach. *Int J Remote Sens* 39: 6805-6825. [https://](https://doi.org/10.1080/01431161.2018.1466076)
888 doi.org/10.1080/01431161.2018.1466076. 2018.
- 889 Hsiao, T., Heng, L., Steduto, P., Rojas-Lara, B., Raes, D., Fereres, E.: AquaCrop-The FAO
890 Crop Model to Simulate Yield Response to Water: III. Parameterization and Testing
891 for Maize. *Agron. J.*, 101(3):448-459. [https:// doi.org/ 10.2134/agronj2008.0218s](https://doi.org/10.2134/agronj2008.0218s).
892 2009.
- 893 Hu, S., Shi, L., Huang, K., Zha, Y., Hu, X., Ye, H., Yang, Q.: Improvement of sugarcane crop
894 simulation by SWAP-WOFOST model via data assimilation. *Field Crop Res.*, 232:
895 49-61. [https:// doi.org/10.1016/j.fcr.2018.12.009](https://doi.org/10.1016/j.fcr.2018.12.009). 2019.
- 896 Huang, Q., Xu, X., Lu, L., Ren, D., Ke, J., Xiong, Y., Huo, Z. and Huang, G.: Soil salinity
897 distribution based on remote sensing and its effect on crop growth in Hetao
898 Irrigation District. *Transactions of the Chinese Society of Agricultural Engineering*,
899 34:102-109. 2018.
- 900 Kendy, E., Gérard-Marchant, P., Walter, M. T., Zhang, Y., Liu, C., and Steenhuis, T.S.: A
901 soil-water-balance approach to quantify groundwater recharge from irrigated
902 cropland in the North China Plain. *Hydrol. Process.*, 17:2011-2031. [https://](https://doi.org/10.1002/hyp.1240)
903 doi.org/10.1002/hyp.1240. 2003.
- 904 Leube, P. C., : Temporal moments revisited: Why there is no better way for physically
905 based model reduction in time, *Water Resour Res*, 48(11): W11527. [https://](https://doi.org/10.1029/2012WR011973)
906 doi.org/10.1029/2012WR011973 2012.
- 907 Li, J., Pu, L., Han, M., Zhu, M., Zhang, R., Xiang, Y.: Soil salinization research in China:
908 Advances and prospects, *J Geogr Sci*, 24(5), 943-960. [https:// doi.org/](https://doi.org/10.1007/s11442-014-1130-2)
909 [10.1007/s11442-014-1130-2](https://doi.org/10.1007/s11442-014-1130-2) .2014
- 910 Li, X., Zhao, Y., Xiao, W., Yang, M., Shen, Y., Min, L.: Soil moisture dynamics and
911 implications for irrigation of farmland with a deep groundwater table. *Agr. Water*
912 *Manage.*, 192:138-148. [https:// doi.org/ 10.1016/j.agwat.2017.07.003](https://doi.org/10.1016/j.agwat.2017.07.003).2017.



- 913 Liu, J.: A GIS-based tool for modelling large-scale crop-water relations. *Environ Modell*
914 *Softw.* 24(3): 411-422. [https:// doi.org/ 10.1016/j.envsoft.2008.08.004](https://doi.org/10.1016/j.envsoft.2008.08.004). 2009.
- 915 Liu, Z., Wang, X., Huo, Z, Steenhuis, T.S.: A unique vadose zone model for shallow
916 aquifers: the Hetao irrigation district, China. *Hydrol Earth Syst Sc.* 23(7):3097-3115.
917 [https:// doi.org/ 10.5194/hess-23-3097-2019](https://doi.org/10.5194/hess-23-3097-2019). 2019.
- 918 Luo, Y., and Sophocleous, M.: Seasonal groundwater contribution to crop-water use
919 assessed with lysimeter observations and model simulations. *J. Hydrol.*
920 389:325-335. [https:// doi.org/10.1016/j.jhydrol.2010.06.011](https://doi.org/10.1016/j.jhydrol.2010.06.011). 2010.
- 921 Ma, Y., Feng, S., and Song, X.: A root zone model for estimating soil water balance and
922 crop yield responses to deficit irrigation in the North China Plain. *Agr. Water Manage.*,
923 127:13-24. [https:// doi.org/10.1016/j.agwat.2013.05.011](https://doi.org/10.1016/j.agwat.2013.05.011). 2013.
- 924 Moriasi, D. N., Arnold, J. G., Van Liew, M. W., Bingner, R. L., Harmel, R. D., Veith, T. L.:
925 Model evaluation guidelines for systematic quantification of accuracy in watershed
926 simulations. *T ASABE*, 50(3): 885-900. 2007.
- 927 Nash, J.E., and Sutcliffe, J.V.: River flow forecasting through conceptual models part I – a
928 discussion of principles. *J Hydrol.* 10:282-290. 1970.
- 929 Novark, V.: Estimation of Soil-water Extraction Patterns by Roots, *Agr Water Manage*,
930 12(4), 271-278. [https:// doi.org/10.1016/0378-3774\(87\)90002-3](https://doi.org/10.1016/0378-3774(87)90002-3). 1987
- 931 Raes, D., Steduto, P., Hsiao, T., Fereres.: AquaCrop-The FAO Crop Model to Simulate
932 Yield Response to Water: II. Main Algorithms and Software Description, *Agron. J.*,
933 101(3), 438. [https:// doi.org/10.2134/agronj2008.0140s.2009](https://doi.org/10.2134/agronj2008.0140s.2009).
- 934 Regis, R., and Shoemaker, C.: Constrained Global Optimization of Expensive Black Box
935 Functions Using Radial Basis Functions, *J Global Optim*, 31(1), 153-171. [https://
936 doi.org/10.1007/s10898-004-0570-0](https://doi.org/10.1007/s10898-004-0570-0). 2005.
- 937 Ren, D., Xu, X., Hao, Y., and Huang, G.: Modeling and assessing field irrigation water use
938 in a canal system of Hetao, upper Yellow River basin: Application to maize,
939 sunflower and watermelon. *J. Hydrol.* 532:122-139. [https://
940 doi.org/10.1016/j.jhydrol.2015.11.040](https://doi.org/10.1016/j.jhydrol.2015.11.040). 2016.
- 941 Rengasamy, P.: World salinization with emphasis on Australia, *J Exp. Bot.*, 57(5),
942 1017-1023. [https:// doi.org/10.1093/jxb/erj108](https://doi.org/10.1093/jxb/erj108) .2006



- 943 Rhoades, J., Manteghi, N., Shouse, P., Alves, W.: Soil Electrical Conductivity and Soil
944 Salinity: New Formulations and Calibrations, *Soil Sci. Soc. Am. J.*, 53(2): 433-439.
945 [https:// doi.org/ 10.2136/sssaj1989.03615995005300020020x](https://doi.org/10.2136/sssaj1989.03615995005300020020x). 1989.
- 946 Ritter, A., and Muñoz-Carpena, R.: Performance evaluation of hydrological models:
947 Statistical significance for reducing subjectivity in goodness-of-fit assessments. *J*
948 *Hydrol.*, 480:33-45. 2013. [htt p:// doi.org/ 10.1016/j.jhydrol.2012.12. 004](https://doi.org/10.1016/j.jhydrol.2012.12.004). 2013.
- 949 Rosa, R.D., Paredes, P., Rodrigues, G.C., Alves, I, Fernando, R.M., Pereira, L.S., Allen, R.G.:
950 Implementing the dual crop coefficient approach in interactive software. 1.
951 Background and computational strategy. *Agr. Water Manage.*, 103: 8-24. [https://](https://doi.org/10.1016/j.agwat.2011.10.013)
952 doi.org/10.1016/j.agwat.2011.10.013. 2012.
- 953 Sau, F., Boote, K., Bostick, W., Jones, J., Minguez, M.: Testing and improving
954 evapotranspiration and soil water balance of the DSSAT crop models. *Agron. J.*, 96:
955 1243-1257. [https:// doi.org/ 10.2134/agronj2004.1243](https://doi.org/10.2134/agronj2004.1243). 2004.
- 956 Shelia, V., Simunek, J., Boote, K., Hoogenboom, G.: Coupling DSSAT and HYDRUS-1D for
957 simulations of soil water dynamics in the soil-plant-atmosphere system. *J Hydrol*
958 *Hydromech.*, 66(2): 232-245. [https:// doi.org/10.1515/johh-2017-0055](https://doi.org/10.1515/johh-2017-0055). 2018.
- 959 Šimůnek, J., Šejna, M. and van Genuchten, M.T.: The HYDRUS-1D software package for
960 simulating the one-dimensional movement of water, heat, and multiple solutes in
961 variably-saturated media. Version 2.0. IGWMC-TPS-70. Int. Groundwater Modeling
962 Ctr., Colorado School of Mines, Golden. 1998.
- 963 Steduto, P., Hsiao, T., Raes, D., Fereres, E.: AquaCrop-The FAO Crop Model to Simulate
964 Yield Response to Water: I. Concepts and Underlying Principles. *Agron J.*,
965 101(3):426-437. [https:// doi.org/10.2134/agronj2008.0139s](https://doi.org/10.2134/agronj2008.0139s). 2009.
- 966 Steenhuis, T., Richard, T., Parlange, M., Aburime, S., Geohring, L., Parlange, J.: Preferential
967 Flow Influences on Drainage of Shallow Sloping Soils. *Agr Water Manage.*,
968 14(1-4):137-151. [https:// doi.org/ 10.1016/0378-3774\(88\)90069-8](https://doi.org/10.1016/0378-3774(88)90069-8). 1988.
- 969 Uehara, G.: Technology-transfer in the tropics. *Outlook Agr.*, 18(1): 38-42. [https://](https://doi.org/10.1177/003072708901800107)
970 [doi.org/ 10.1177/003072708901800107](https://doi.org/10.1177/003072708901800107). 1989.
- 971 Van Diepen, C., Wolf, J., van Keulen, H., Rappoldt, C.: WOFOST A STIMULATION MODEL
972 OF CROP PRODUCTION. *Soil Use and Management*, 5(1): 16-24. 1989.



- 973 Wallender, W. , Tanji, K. : Agricultural salinity assessment and management. Agricultural
974 salinity assessment and management. Ed.2. American Society of Civil Engineers
975 (ASCE), Reston, USA. University of California-Davis, USA.: xxx+1094pp. 2011.
- 976 Wang, X., Huang, G., Yang, J., Huang, Q., Liu, H., Yu, L.: An assessment of irrigation
977 practices: Sprinkler irrigation of winter wheat in the North China Plain. *Agr Water*
978 *Manage.*, 159: 197-208. [https:// doi.org/ 10.1016/j.agwat.2015.06.011](https://doi.org/10.1016/j.agwat.2015.06.011). 2015.
- 979 Wang, J., Huang, G., Zhan, H., Mohanty, B., Zheng, J., Huang, Q., Xu, X.: Evaluation of soil
980 water dynamics and crop yield under furrow irrigation with a two-dimensional flow
981 and crop growth coupled model. *Agr Water Manage.*, 141: 10-22. [https:// doi.org](https://doi.org/10.1016/j.agwat.2014.04.007)
982 [/10.1016/j.agwat.2014.04.007](https://doi.org/10.1016/j.agwat.2014.04.007). 2014.
- 983 Williams, J., Jones, C., Kiniry, J., and Spanel, D.: The EPIC Crop Growth Model. *T. ASAE*,
984 32:479-511. 1989.
- 985 Williams, W. D., Salinisation: A major threat to water resources in the arid and semi-arid
986 regions of the world, *Lakes Reservoirs Research and Management*, 4(3-4), 85-91.
987 [https:// doi.org/10.1046/j.1440-1770.1999.00089.x](https://doi.org/10.1046/j.1440-1770.1999.00089.x). 1999.
- 988 Willcox, K., and Paire J.: Balanced Model Reduction via the Proper Orthogonal
989 Decomposition, *AIAA J*, 40(11), 2323-2330. [https:// doi.org/10.2514/2.1570](https://doi.org/10.2514/2.1570).
990 2002.
- 991 Xu, X., Sun, C., Qu, Z., Huang, Q., Ramos, T.B., and Huang, G.: Groundwater Recharge and
992 Capillary Rise in Irrigated Areas of the Upper Yellow River Basin Assessed by an
993 Agro-Hydrological Model. *Irrig. Drain.*, 64:587-599. [https://](https://doi.org/10.1002/ird.1928)
994 doi.org/10.1002/ird.1928. 2015.
- 995 Xu, X., Sun, C., Huang, G., Mohanty, B.: Global sensitivity analysis and calibration of
996 parameters for a physically-based agro-hydrological model. *Environ Modell Softw.*,
997 83: 88-102. [https:// doi.org/10.1016/j.envsoft.2016.05.013](https://doi.org/10.1016/j.envsoft.2016.05.013). 2016.
- 998 Xu, X., Huang, G., Sun, C., Pereira, L., Ramos, T., Huang, Q., Hao, Y.: Assessing the effects
999 of water table depth on water use, soil salinity and wheat yield: Searching for a
1000 target depth for irrigated areas in the upper Yellow River basin. *Agr Water Manage*,
1001 125: 46-60. [https:// doi.org/10.1016 /j.agwat.2013.04.004](https://doi.org/10.1016/j.agwat.2013.04.004). 2013.
- 1002 Xu, X., Huang, G., Qu, Z., and Pereira, L.S.: Assessing the groundwater dynamics and
1003 impacts of water saving in the Hetao Irrigation District, Yellow River basin. *Agr*



- 1004 Water Manage., 98:301-313. [https:// doi.org/10.1016/j.agwat.2010.08.025](https://doi.org/10.1016/j.agwat.2010.08.025).
1005 2010.
- 1006 Xue, J., Huo, Z., Wang, F., Kang, S., and Huang, G.: Untangling the effects of shallow
1007 groundwater and deficit irrigation on irrigation water productivity in arid region:
1008 New conceptual model. *Sci. Total Environ.*, 619-620:1170-1182. [https://](https://doi.org/10.1016/j.scitotenv.2017.11.145)
1009 doi.org/10.1016/j.scitotenv.2017.11.145 2018.
- 1010 Yang, X., Chen, Y., Pacenka, S., Gao, W., Ma, L., Wang, G., Yan, P., Sui, P., and Steenhuis, T.
1011 S.: Effect of diversified crop rotations on groundwater levels and crop water
1012 productivity in the North China Plain, *J. Hydrol.*, 522, 428–438,
1013 <https://doi.org/10.1016/j.jhydrol.2015.01.010>, 2015a.
- 1014
- 1015 Yang, X., Chen, Y., Pacenka, S., Gao, W., Zhang, M., Sui, P., and Steenhuis, T. S.: Recharge
1016 and groundwater use in the North China Plain for six irrigated crops for an eleven
1017 year period, *Plos One*, 10, e0115269, <http://doi.org/10.1371/journal.pone.0115269>,
1018 doi.org/10.1371/journal.pone.0115269, 2015b.
- 1019 Yeh, P.J., and Famiglietti, J.S.: Regional groundwater evapotranspiration in Illinois. *J.*
1020 *Hydrometeorol.*, 10:464-478. [https:// doi.org/ 10.1175/2008JHM1018.1](https://doi.org/10.1175/2008JHM1018.1). 2009.
- 1021 Zhang, B., Kang, S., Zhang, L., Du, T., Li, S., Yang, X.: Estimation of seasonal crop water
1022 consumption in a vineyard using Bowen ratio-energy balance method. *Hydrol.*
1023 *Process*, 21(6): 3635-3641. [https:// doi.org/ 10.1002/hyp.6568](https://doi.org/10.1002/hyp.6568).
- 1024 Zhang, F., Zhou, G., Wang, Y., Yang, F., Nilsson, C.: Evapotranspiration and crop
1025 coefficient for a temperate desert steppe ecosystem using eddy covariance in Inner
1026 Mongolia, China. *Hydrol. Process*, 26(3): 379-386. [https:// doi.org/](https://doi.org/10.1002/hyp.8136)
1027 [10.1002/hyp.8136](https://doi.org/10.1002/hyp.8136).